

CALIFA Spectroscopy of the Interacting Galaxy NGC 5394 (Arp 84): Starbursts, Enhanced [NII]6584 and Signs of Outflows and Shocks

Nathan Roche¹ *, Andrew Humphrey¹, Jean Michel Gomes¹, Polychronis Papaderos¹, Patricio Lagos¹, Sebastián F. Sánchez²

¹ *Instituto de Astrofísica e Ciências do Espaço, Universidade do Porto, CAUP, Rua das Estrelas, 4150-762 Porto, Portugal.*

² *Instituto de Astronomía, Universidad Nacional Autónoma de México, A.P. 70-264, 04510, México, D.F.*

23 June 2015

ABSTRACT

We investigate the spiral galaxy NGC 5394, which is strongly interacting with the larger spiral NGC 5395 (the pair is Arp 84), using optical integral-field spectroscopy from the CALIFA survey. Spatially-resolved equivalent-widths, emission-line ratios and kinematics reveal many features related to the interaction, which has reshaped the galaxy. $H\alpha$ maps (with other diagnostic emission lines) show a concentrated central ($r < 1$ kpc) starburst and three less luminous star-forming regions (one knot far out in the northern arm), and we estimate the dust-corrected total star-formation rate as $3.39 \text{ M}_{\odot} \text{ yr}^{-1}$. However, much of the galaxy, especially the outer tidal arms, has a post-starburst spectrum, evidence of a more extensive episode of star-formation a few $\times 10^8$ yr ago, triggered by the previous perigalacticon. The [NII]6584/ $H\alpha$ ratio is high in the nucleus, reaching 0.63 at the centre, which we interpret as related to high electron density ($n_e \simeq 750 \text{ cm}^{-3}$ from the [SII] $\frac{6717}{6731}$ ratio). We find a central region of strong and blueshifted NaI(5890,5896) absorption, indicative of a starburst-driven outflow from the nucleus at an estimated velocity $\sim 223 \text{ km s}^{-1}$. The CALIFA data also show an annular region at radii 2.25–4 kpc from the nucleus, with elevated ratios of [NII], [OI]6300 etc. to the Balmer lines – this is evidence of shock excitation, which might be the result of interaction-triggered gas inflow.

Key words: galaxies: individual: NGC 5394, galaxies:interactions, galaxies: evolution, galaxies:starburst

1 INTRODUCTION

Mergers of two spiral galaxies are one of the most important processes in galaxy evolution, and typically occur in a sequence of stages over several hundred Myr, with successive close passages (perigalactica) of the pair, multiple bursts of star-formation, and complex morphological transformations preceding the final coalescence into a single galaxy (which could become an elliptical or lenticular). Interacting galaxies at any stage can be well studied by integral field spectroscopy (IFS), which may reveal both the current activity and recent history within each resolution element.

NGC 5394 and NGC 5395 are an interacting close pair of spirals, which appear to be destined to merge. This well-known system was included in the Arp (1966) catalog of pe-

culiar galaxies under the single name of Arp 84, and studied further by Arp (1969). On account of its shape it has also been called the Heron Galaxy, with the larger NGC 5395 being the ‘body and wings’ and the two-armed, northern NGC 5394 the ‘neck, head and beak’; this is well-depicted on the Gran Telescopio Canarias gallery image (Fig 1).

NGC 5394, a barred spiral seen almost face-on and classed as SB(s)b-pec, appears relatively symmetric, but its structure is unusual and greatly modified by the interaction. Within its compact disk it has a small, bright nucleus and 3 arms (double on the west) and beyond the disk (radii $r > 13$ arcsec out to ~ 40 arcsec) a distinct and much larger system of two long arms extending north and south, the southern arm reaching NGC 5395.

The Arp 84 system is described in some detail by Kaufman et al. (1999), hereafter K99, who observed in $H\alpha$ with a Fabry-Perot. NGC 5394 and 5395 have a mass and luminos-

* nathan.roche@astro.up.pt

ity ratio about 1:4, projected separation 28 kpc, and rotate anticlockwise and clockwise respectively, so that their arms are trailing. The interaction (an orbit approximately in the sky plane) is prograde with respect to the rotation of NGC 5394, but retrograde and inclined for NGC 5395. NGC 5394 has strong H α emission (indicating star-formation) from the nucleus (2.2×10^{-13} erg cm $^{-2}$ s $^{-1}$ from Keel et al. 1985) and more from a region in the SW of the disk (the inner western arm) and two bright spots on the inner and outer northern arm. K99’s radio observations give the neutral hydrogen (HI) mass in NGC 5394 as $7.3 \times 10^8 M_\odot$, and the CO data (tracing molecular hydrogen) show a dense concentration ($> 10^9 M_\odot$) of H $_2$ in the nucleus. K99 describe NGC 5394 as ‘post-ocular’ in that it resembles the ‘eye-shaped’ interacting galaxies IC 2163 and NGC 2535 but is at a slightly later stage where ‘the eye-shaped oval has evolved into inner spiral arms and most of the gas has fallen into the central region, where it fuels a starburst’. K99 reported some evidence for a low-velocity outflow from asymmetry of the H α line (a possible blueshifted component) and small (~ 10 km s $^{-1}$) distortions in the H α velocity map (NE of the nucleus); unconfirmed but will be investigated here.

Kaufman et al. (2002), hereafter K02, performed further CO observations and compare with several other passbands. They estimate NGC 5394 is inclined $15^\circ \pm 2$ to the sky plane, discuss evidence (e.g. $60\mu\text{m}$ flux) the H α flux is reduced by as much as an order of magnitude by internal dust extinction, and on this basis estimate the total (dust-corrected) star-formation rate (SFR) as $6 \pm 2 M_\odot\text{yr}^{-1}$ (with no evidence of an AGN contribution). The star-formation closely traces the HI and H $_2$ distributions – all three are concentrated in the central kpc, but also the disk is ‘lopsided, with more HI, CO, and H α emission coming from the western or southwestern side’, and there was speculation that this resulted from a west-vs-east time lag in the formation of disk arms and subsequent infall of gas to the nucleus. They estimate a molecular/atomic ratio $M(\text{H}_2)/M(\text{HI}) = 2.5\text{--}2.7$ (even with a lower CO–H $_2$ conversion factor applied for starbursts), very high compared to 0.86 for NGC 5395, which contains much more HI ($> 10^{10} M_\odot$), and the average ratio of 0.28 for spiral galaxies (Casoli et al. 1998).

Puerari et al. (2005) studied the morphology of both galaxies in the near-infrared (JHK), and fit (in the K -band) a bulge profile with $r_{\text{eff}} = 3.12$ arcsec plus a disk of scale length $h = 6.35$ arcsec for NGC 5394, which is ‘more compact than normal galaxies’. From the disturbed, Cartwheel-like structure of NGC 5395 they conclude the system is undergoing a strong interaction, a ‘collision rather than a grazing encounter’. Kaneko et al. (2013) again study the system in CO and depict the contrast between the compact, nucleated, H $_2$ -rich NGC 5394 and the ring-like and HI-rich 5395.

Smith et al. (2007) observed the system from 3.6 to $24\mu\text{m}$ in a *Spitzer* survey of Arp-catalog galaxies: most emission from NGC 5394 is from the compact nucleus and the *Spitzer* images also show the prominent bright spot (H α source) out in the northern arm. Higdon et al. (2014) describe this hotspot (‘N1’) as an ‘intergalactic star-forming object’ with a $8\mu\text{m}$ flux of 2.626 ± 0.015 mJy, $\sim 1\%$ that of the whole galaxy (279.8 ± 3.8 mJy), and in the mid-IR it is also detected in [NeII], [NeIII], [SIII] and PAHs.

Note that the SFRs estimated from observable quantities will generally depend on the assumed initial mass func-

tion (IMF), e.g. the SFR from K02 assumed a Salpeter IMF, whereas equivalent SFR estimates based on the Chabrier or Kroupa IMFs, with fewer low-mass stars, will be 40–45% lower. Lehmer et al. (2010) estimated a (Kroupa IMF) SFR of $9.9 M_\odot\text{yr}^{-1}$ for the whole Arp 84 system, simply from the infra-red luminosity of $10^{11} M_\odot\text{yr}^{-1}$, and found its X-ray luminosity from *Chandra* data consistent with the typical L_x – SFR relation of LIRGs, meaning it can be accounted for by X-ray binaries without requiring AGN. Howell et al. (2010) estimated a higher SFR of $20.99 M_\odot\text{yr}^{-1}$ by including the unobscured component traced by far-UV luminosity (*GALEX*) as well as the infra-red luminosity and modelling with the Salpeter IMF.

Lanz et al. (2013) combined fluxes in many bands from FUV (*Galex*) to FIR (*Herschel*) for a sample of interacting galaxies and fitted the SEDs with a program MAGPHYS, which assumed a Chabrier IMF and gives a SFR averaged over the past 100 Myr. For NGC 5394 and 5395, they estimate SFRs of 1.54 and $3.69 M_\odot\text{yr}^{-1}$, and found some difference in their SEDs, with NGC 5394 having relatively more $12\text{--}60\mu\text{m}$ flux and higher dust temperatures (23.2K in the cold component) in comparison to 5395 (with 19.7 K) and the non-interacting control sample (about 19K). This is consistent with NGC 5394 experiencing a strong (‘stage 4’), and late-stage interaction, with star-formation more centrally concentrated than in the more massive companion. Stellar masses are estimated as 4.79 and $15.14 \times 10^{10} M_\odot$.

In this paper we investigate the spatially-resolved properties and history of NGC 5394, especially the effects of the interaction, using new integral field spectroscopy from the Calar Alto Legacy Integral Field Area (CALIFA) survey (Sánchez et al. 2012; Husemann et al. 2013). CALIFA has already been the basis for a number of papers on global properties and on in-depth studies of particular galaxies, with which we can compare – e.g. the famous ‘playing Mice’ interacting pair NGC 4676A/B (Wild et al. 2014), and studies of metallicity gradients in typical spirals and mergers (Sánchez et al. 2014; Barrera-Ballesteros et al. 2015). We will also compare with models of emission-line ratios in star-forming galaxies (e.g. Kewley et al. 2013) and in shocks (Allen et al. 2008); and simulations of galaxy mergers (e.g. Barnes et al. 2004, Struck et al. 2005, Torrey et al. 2012).

From the CALIFA catalog, the J2000 co-ordinates of NGC 5394 are R.A. 13:58:33.19 and Dec +37:27:13.11 and the heliocentric optical recession velocity is 3457 km s^{-1} ($z = 0.01153$); the velocity relative to the local standard of rest (Virgo cluster) is given as a slightly greater 3688 km s^{-1} (corresponding to $z = 0.01230$). For $H_0 = 70 \text{ km s}^{-1}\text{Mpc}^{-1}$, $\Omega_M = 0.27$, $\Omega_\Lambda = 0.73$ (assumed throughout) the Virgo velocity corresponds to a distance modulus 33.64 mag (the value listed in the CALIFA catalog) and an angular diameter distance 52 Mpc, so that 1 arcsec subtends 252 parsec. In Section 2 of this paper we describe the data, in Section 3 the distribution of star-formation activity, in Section 4 and 5 diagnostic line ratios and metallicity, in Section 6 the line-of-sight kinematics and and Section 7 discuss the history of the interaction (summarising in Section 8).

2 CALIFA OBSERVATIONS

Our data set for NGC 5394 comes from the first CALIFA public data release (DR1; Husemann et al. 2013), which consists of optical datacubes (image \times wavelength) for the first 100 (of what will be eventually 600+) galaxies in the survey, now updated with Data Release 2 (García-Benito et al. 2015). CALIFA observations are obtained with the integral-field spectrograph PMAS/PPAK mounted on the 3.5m telescope at the Calar Alto observatory. The PPAK unit contains 331 densely packed optical fibres arranged in a hexagonal area of 74×65 arcsec, to sample an astronomical object at 2.7 arcsec per fibre, with a filling factor of 65% due to inter-fibre gaps.

The CALIFA galaxy sample is selected from the Sloan Digital Sky Survey (SDSS) DR7 catalog, simply on the basis of redshift ($0.005 < z < 0.03$) and apparent size (angular isophotal diameter $45 < D_{25} < 80$ arcsec), so that each galaxy fitted within, while filling most of, a single field-of-view. This means the survey covers a very wide range of morphological type, absolute magnitude, stellar mass, star-formation rate, colour, etc. (Walcher et al. 2014). NGC 5395 was not targeted in CALIFA as its apparent size is more than twice NGC 5394 (radii $R_{K20} = 34$ and 71 arcsec; Kaneko et al. 2013) and exceeds a single field-of-view, so this analysis is limited to the more compact galaxy.

Each galaxy was observed with two spectrograph configurations, (i) the V500 grating covering the wavelength range 3745–7500Å with a spectral resolution of 6.0Å (FWHM), and (ii) the V1200 grating covering 3650–4840Å with a spectral resolution of 2.3Å (FWHM). Exposure times are 900 sec on each galaxy with V500 and 3×600 s with V1200, and the respective 3σ limits for detection of a narrow emission line are 1.0 and 0.6×10^{-17} ergs cm $^{-2}$ s $^{-1}$. Initial processing of these data generated two (V500 and V1200) data cubes for each galaxy, which are supplied on the CALIFA website (califa.caha.es) calibrated in units of Å and 10^{-16} erg cm $^{-2}$ s $^{-1}$ Å $^{-1}$ and rebinned into a grid of 1 arcsec spatial pixels. As the spectrograph fibre diameter is 2.7 arcsec, the effective spatial resolution is lower, with FWHM from 3 to 4 arcsec. The cubes are 78×73 (spatial) $\times 1877$ (spectral) with $d\lambda = 2.0$ Å for V500, and $78 \times 73 \times 1701$ with $d\lambda = 0.7$ Å for V1200.

In this paper we concentrate mostly on the V500 spectra which contain the lines of interest. We have analyzed the datacubes using a locally developed software pipeline called Porto3D (Papaderos et al. 2013, Gomes et al. 2015), which effectively separates out the stellar and nebular (emission-line) components of each spatial pixel’s spectrum. The stellar component is fitted with a set of model stellar spectra, with a wide range of ages, using the Starlight package (Cid Fernandes et al. 2013). The total stellar mass is estimated from the Porto3D fit as $4.6 \times 10^{10} M_{\odot}$ (for Salpeter IMF). For a list of spectral lines, the program generates 2D maps of emission-line flux, equivalent width, velocity offset (red or blueshift), and the equivalent widths for any stellar absorption lines (for Balmer lines H β – γ – δ there may be narrow emission within broader absorption; as was seen for this galaxy by Arp 1969). Further maps show stellar properties estimated from the model fits, such as mean stellar age and metallicity (mass and luminosity weighted). One line map, for [OI]6300, appeared mildly contaminated by the sky line

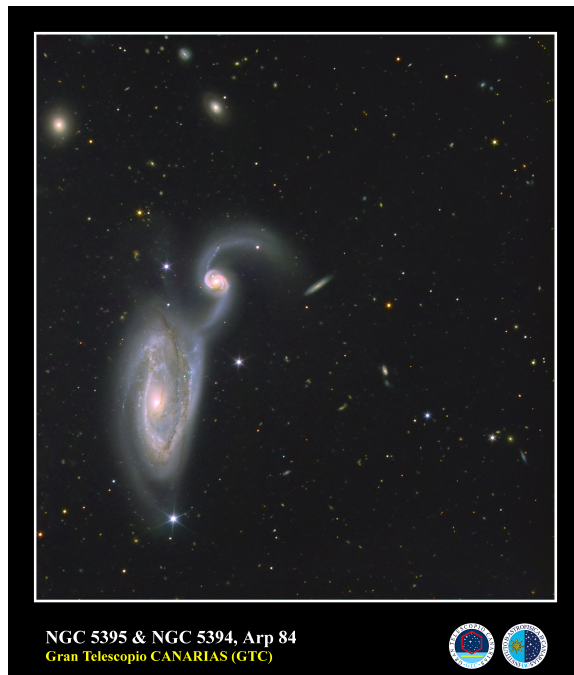


Figure 1. Gran Telescopio Canarias public gallery image of Arp 84, NGC 5394 (north) 5395 (south). From www.gtc.iac.es/multimedia/media/GTC_ARP84.jpg

[OI]6364 (de-redshifted to 6291Å), so to exclude this a new flux map was computed summing 6297–6307Å only.

3 MAPPING THE STAR-FORMATION

Figure 2 shows the CALIFA image of NGC 5394 in the continuum at 6390–6490Å, just blueward of H α , where it appears near-symmetrical, but the emission lines will reveal a much more complex picture. The H α emission line is the best tracer of the current star-formation rate (SFR). CALIFA maps of the H α flux and equivalent width (EW, here in the rest-frame) show (Fig 3) the star-formation is concentrated in four distinct regions, the nucleus ($r < 4$ arcsec or 1 kpc), a region in the SW of the disk (identified by K99 as the inner of two western spiral arms) and two compact ‘hotspots’ in the inner and outer northern tidal arm (see also Fig 4 of K99). Peak H α equivalent widths are 52.8, 70.3 and 54.1Å for the nucleus, SW disk and inner-N hotspot, with the highest of all, 106.7Å for the far-N hotspot, but the nucleus produces by far the greatest H α luminosity.

Arp (1969) described an ‘unusually sharply defined string of condensations coming out of the companion on the inside of the northern arm’. This ‘string’ is visible on the GTC image, and the inner-N and far-N H α -emitting hotspots can be identified with the knots at either end. Probably the intermediate knots are recent sites of star-formation, which now continues only at the extremities. There is lower intensity H α emission distributed over the whole disk (out to $r \simeq 12$ arcsec), but almost none from the tidal arms outside of the two hotspots.

To illustrate some of the diversity within this galaxy, Fig 4 compares small-aperture CALIFA spectra of the nucleus, the far-N hotspot (averaged over the central 5 pixels

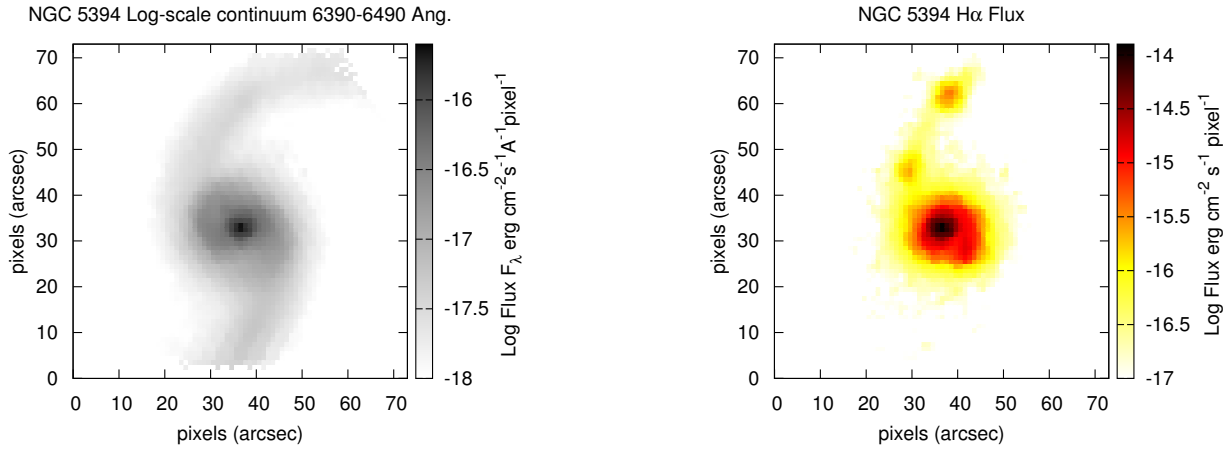


Figure 2. NGC5394 red-band continuum map from CALIFA data. North is up and East is left, as in all figures.

of each) and a region in the southern arm (averaged over 14 pixels). Wavelengths 5508–5522 Å, 6222–6236 Å and 6285–6295 Å (galaxy restframe) are severely affected by strong sky OI lines (observed at 5577.3, 6300.3 and 6363.8 Å), and are masked out in the plots and model fitting. The nucleus has the strong emission lines expected for a starburst, although [OIII]5007 is relatively weak and the continuum relatively red (i.e. redder than flat in F_ν). The two outer regions are bluer and the N hotspot has strong emission lines, while the S arm is not only passive but may be post-starburst on the basis of strong Balmer absorption lines ($EW > 5\text{ Å}$). The nucleus has notable differences in emission-line ratios compared to the hotspot, with higher [NII]6584/H α and lower [SII]6717/[SII]6731.

SFRs locally and for the whole galaxy can be estimated by summing the H α fluxes, but there is evidence (K02) the emission lines are substantially attenuated by internal dust. For star-forming HII regions the intrinsic flux ratio of H α /H β (when corrected for stellar absorption as here) is expected to be 2.86 (from ‘case B’ models with $T_e \sim 10^4\text{ K}$), but the observed ratio is increased in proportion to the dust-reddening. Using the extinction law of Calzetti et al. (2000), supported by the more recent results of Wild et al. (2011), a dust-corrected H α flux is estimated for each individual pixel as $F(\text{H}\alpha)_{\text{corr}} \simeq F(\text{H}\alpha)_{\text{obs}} [\text{H}\alpha/2.86\text{H}\beta]^{2.615}$. Here this dust correction is only applied for pixels where the statistical error $\sigma(\text{H}\alpha/\text{H}\beta) < 1.0$, which includes all of the disk and the star-forming regions in the northern arm (the other pixels are included in the H α flux summations but uncorrected). Figure 5 shows a map of the H α dust extinction, which is greatest for the nuclear region (2.32 mag).

To depict the IFS data (without defeating the object by too much spatial binning) can be challenging and three methods are used here, 2D maps, radial profiles averaged in circular annuli, and we also divide the galaxy into 7 regions, shown on Fig 6. Table 1 gives the observed and dust-corrected H α fluxes, summed over each of the 7 regions and for the whole galaxy (for the integrated H α the estimated extinction is 1.98 magnitudes). Fig 7 shows the integrated

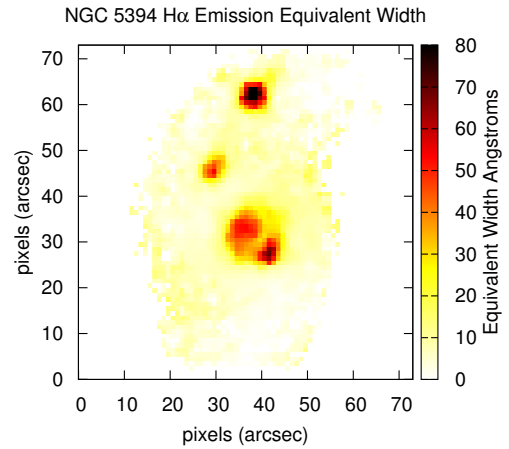


Figure 3. Map of (log scale) H α emission-line flux arcsec^{-2} (above) and equivalent width in Å (below).

CALIFA spectra of each region (note they have different areas), which will be model-fitted in a later Section.

From the dust-corrected fluxes, H α luminosities in erg s^{-1} are calculated using the distance modulus 33.64 mag. A star-formation rate in solar masses (M_\odot) per year can then be estimated as $4.4 \times 10^{-42} L(\text{H}\alpha)$ (e.g. Sobral et al. 2013); this conversion factor is for the Chabrier IMF. We estimate $3.39 M_\odot \text{yr}^{-1}$ for the whole galaxy. For the Salpeter IMF (with more low mass stars) the SFR would be $7.9 \times 10^{-42} L(\text{H}\alpha)$ (Kennicutt et al. 1998) giving $6.09 M_\odot \text{yr}^{-1}$, in agreement with the K02 estimate $6 \pm 2 M_\odot \text{yr}^{-1}$. In comparison, for the Mice galaxies (each larger and about twice as massive as NGC 5394), Wild et al. (2014) estimated SFRs $6.2 M_\odot \text{yr}^{-1}$ for NGC 4676A and $2.3 M_\odot \text{yr}^{-1}$ for NGC 4676B (correcting for dust using UV and mid-infrared fluxes).

We estimate the far-N hotspot accounts for 0.9% of the galaxy’s SFR, the same as its fraction of the $8\mu\text{m}$ flux (2.626/279.8 mJy) in *Spitzer* observations (Higdon et al. 2014). Such features are not unexpected e.g. the ‘ocular’ IC 2163 has at least 9 star-forming clumps spaced around the

Region	$F(\text{H}\alpha)_{\text{obs}}$ $\text{erg cm}^{-2}\text{s}^{-1}$	$F(\text{H}\alpha)_{\text{corr}}$ $\text{erg cm}^{-2}\text{s}^{-1}$	$L(\text{H}\alpha)_{\text{corr}}$ erg s^{-1}	SFR_{corr} $\text{M}_{\odot}\text{yr}^{-1}$	$\frac{[\text{NII}]}{\text{H}\alpha}$	$\frac{[\text{OIII}]}{\text{H}\beta}$	$\frac{[\text{SII}]}{\text{H}\alpha}$	$\frac{[\text{OI}]}{\text{H}\alpha}$	$[\text{SII}]_{\frac{6717}{6731}}$
Nucleus	1.981×10^{-13}	1.681×10^{-12}	5.749×10^{41}	2.53	0.592	0.273	0.288	0.023	1.069
SW disk	3.776×10^{-14}	1.547×10^{-13}	5.290×10^{40}	0.23	0.452	0.262	0.296	0.031	1.375
Outer disk	9.414×10^{-14}	3.603×10^{-13}	1.232×10^{41}	0.54	0.551	0.407	0.343	0.043	1.351
Inner-N hotspot	5.273×10^{-15}	1.154×10^{-14}	3.946×10^{39}	0.017	0.466	0.425	0.289	0.033	1.301
Far-N hotspot	7.257×10^{-15}	2.031×10^{-14}	6.946×10^{39}	0.031	0.408	0.280	0.270	0.019	1.526
N arm	1.161×10^{-14}	1.578×10^{-14}	5.396×10^{39}	0.024					
S arm	8.861×10^{-15}	1.088×10^{-14}	3.721×10^{39}	0.016					
Whole Galaxy	3.629×10^{-13}	2.242×10^{-12}	7.710×10^{41}	3.39	0.562	0.368	0.312	0.033	1.191

Table 1. Integrated $\text{H}\alpha$ luminosities for each of 7 regions of the galaxy NGC 5394 (Fig 6); fluxes and luminosities corrected for dust using the Balmer decrement; star-formation rates derived from the corrected $L(\text{H}\alpha)$ (Chabrier IMF); and several important line ratios from integrated, uncorrected fluxes (not shown for tidal arms as the line fluxes are so low).

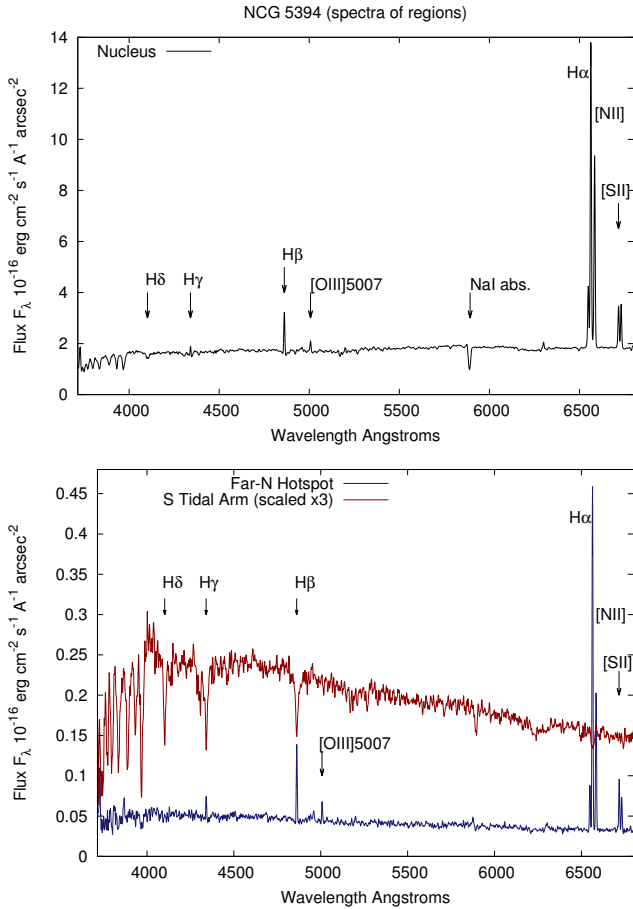


Figure 4. CALIFA V500-grating spectra in 3 different regions of NGC 5394, the nucleus, the far-north star-forming hotspot (averaged over central 5 pixels), and the (post-starburst) southern tidal arm.

‘eye’, with similar $\text{H}\alpha$ and $8\mu\text{m}$ fluxes (Kaufman et al. 2012). In NGC 5394, star-formation is now concentrated in the nucleus, with 75% at $r < 1$ kpc. Fig 8 shows the observed and dust-corrected $\text{H}\alpha$ flux profile, averaged in circular annuli centred on the nucleus (the peak at $r = 29$ arcsec is the far-N hotspot), and also profiles centred on the far-N hotspot itself out to $r = 10$ arcsec only. The nucleus and hotspot are very different in luminosity but are concentrated star-

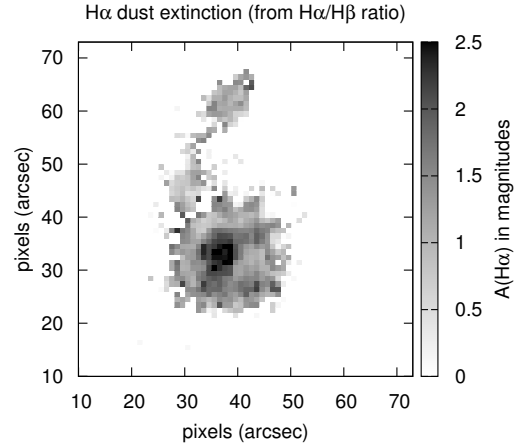


Figure 5. $\text{H}\alpha$ dust extinction as estimated from the Balmer decrement $\text{H}\alpha/\text{H}\beta$ using the Calzetti (2000) law.

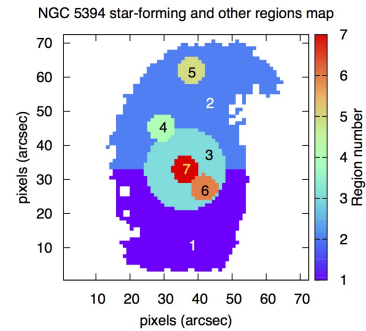


Figure 6. Map of regions the galaxy is divided into for the analysis in Table 1: (1) S Arm (2) N arm (3) Outer disk (4) Inner-N hotspot (5) Far-N hotspot (6) SW disk (7) Nucleus

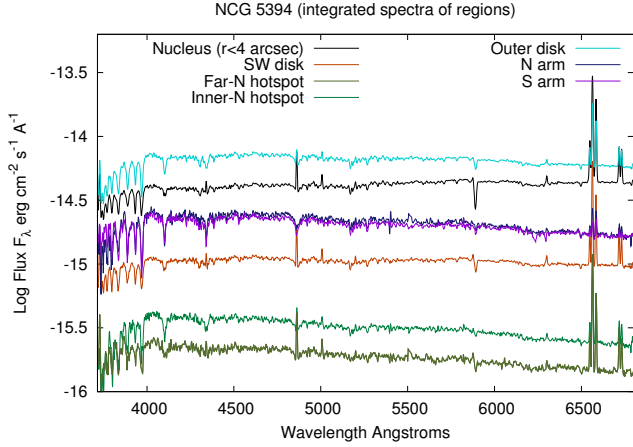


Figure 7. CALIFA V500-grating spectra integrated over 7 regions of NGC 5394 as shown in Fig 6, on a log scale.

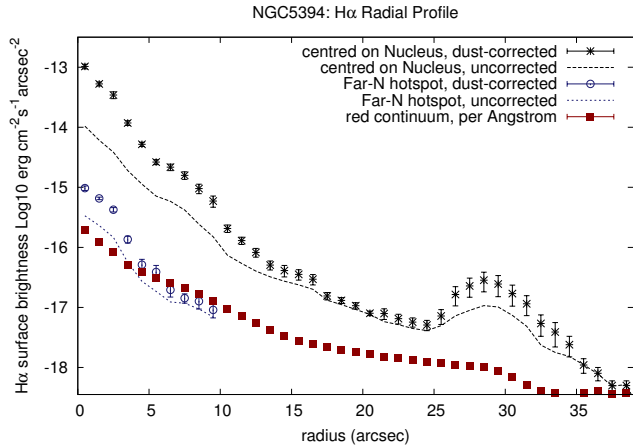


Figure 8. Radial profile of $H\alpha$ emission, centred on the nucleus, as observed and as corrected for dust using the $H\alpha/H\beta$ ratio. Also shown, at $r < 10$ arcsec, the profile of the hotspot in the northern arm, and for comparison, the shallower profile of the red continuum (6390–6490 Å) in flux \AA^{-1} .

formation regions and have similarly steep profiles. In the continuum, the profile of the galaxy is shallower, closer to an exponential, without the steepening at $r \leq 10$ arcsec. The central star-formation density is very high (higher than in NGC 4676A), with an integrated $H\alpha$ flux 1.03×10^{-13} (observed) or 9.39×10^{-13} (corrected) in the central 14 pixels (0.889 kpc^2); the latter corresponds to $1.6 \text{ M}_\odot \text{yr}^{-1} \text{kpc}^{-2}$.

4 LINE RATIOS

We examine a number of other diagnostic lines and ratios. Firstly, the equivalent width of the $H\delta$ stellar absorption line (Fig 9) is high ($6\text{--}9\text{\AA}$) over most of the galaxy area, especially the tidal arms. An $\text{EW}_{\text{abs}}(H\delta) > 5\text{\AA}$ is considered diagnostic of a post-starburst region or galaxy (e.g. Goto 2008) and is caused by an enhancement in the fraction of A-type stars, which on the basis of stellar lifetimes implies they formed in a period of increased star-formation between 100 Myr and 1 Gyr ago. Only in the active star-forming

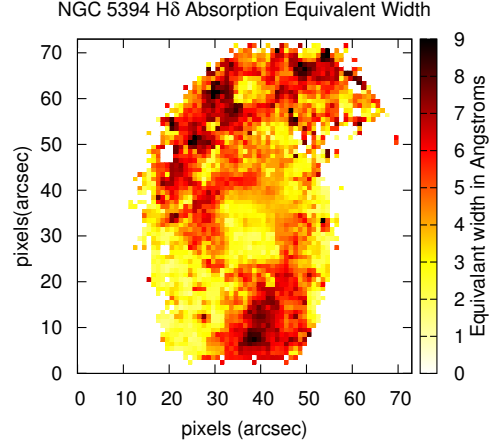


Figure 9. Map of $H\delta$ absorption-line equivalent width.

($H\alpha$ -emitting) regions is $\text{EW}(H\delta)$ reduced to a more typical $3\text{--}4\text{\AA}$, presumably because the A-type spectrum is mixed with even younger OB stars. This shows NGC 5394 is very much a post-starburst galaxy with the earlier burst more spatially extended than the current activity.

Of much importance in identifying AGN and other sources of high excitation, and estimating metallicity, are the line ratios $[\text{NII}]\lambda 6584/H\alpha$ (the N2 index) and $[\text{OIII}]\lambda 5007/H\beta$ (the O3 index). These and the other line ratios considered here (except $H\alpha/H\beta$) are almost insensitive to dust because the two wavelengths are very close. For the galaxy as a whole $\text{O3} = 0.368$ and $\text{N2} = 0.562$. Fig 10 and 11 show the ratio maps, and Fig 12 the radial profiles (centred on the nucleus, and for comparison at the far-N hotspot). Many pixels, generally in the outer galaxy where emission lines are weak or absent, give very noisy or meaningless ratios, and these maps and profiles include only pixels where the ratio measurement is $> 3\sigma$.

The O3 ratio is low at 0.25–0.3 within the main star-forming regions, with no increase at the centre (only 0.254 for the central 4 pixels), so gives no evidence for an AGN. In contrast, N2 is strongly peaked at the nucleus, 0.619 for the central 4 pixels and 0.629 at the highest pixel, but falls to 0.52 at $r = 6$ arcsec, and 0.41 in the far-N hotspot, which is more typical for star-forming regions. However, at the outer edge of the disk the mean N2 increases again to > 0.6 , and in many pixels here it is even higher than at the centre, with ratios 0.65–0.85. At the same radii there is an increase in O3, and to some extent in $[\text{SII}]/H\alpha$ and $[\text{OI}]/H\alpha$. We find an outer region of enhanced line ratios forming an irregular annulus, mostly between $r \simeq 9$ and 16 arcsec. The N2 ratios in both the nucleus and this outer region exceed the $\log(\text{N2}) = -0.25$ upper limit of typical star-formation (e.g. the Kauffmann et al. 2003 divide).

CALIFA data for the Mice galaxies (Wild et al. 2014) showed large biconical regions in both disks with $\text{N2} > -0.25$ dex (0.56) up to $\text{N2} \simeq 1$, with spatially matching high values for the ratios $[\text{OI}]\lambda 6300/H\alpha$ (with 0.1–0.25) and $[\text{SII}]/H\alpha$ (with 0.6–1.0), and (in 4676A) O3 (which ranged from 1–4). These high ratios and the bicone morphology

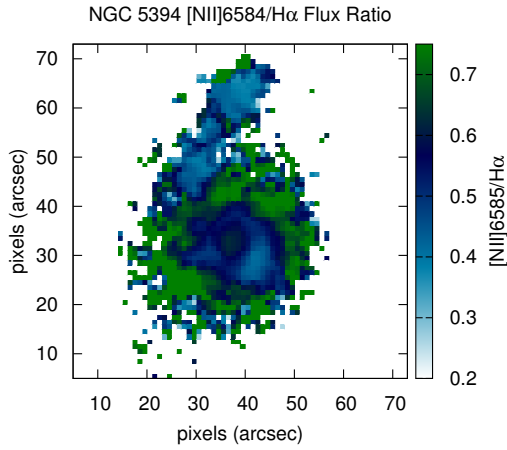


Figure 10. Map of [NII]/H α ratio (N2 index).

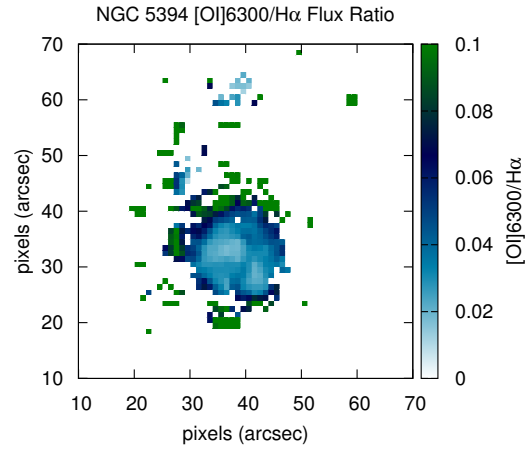


Figure 13. Map of [OI]6300/H α ratio.

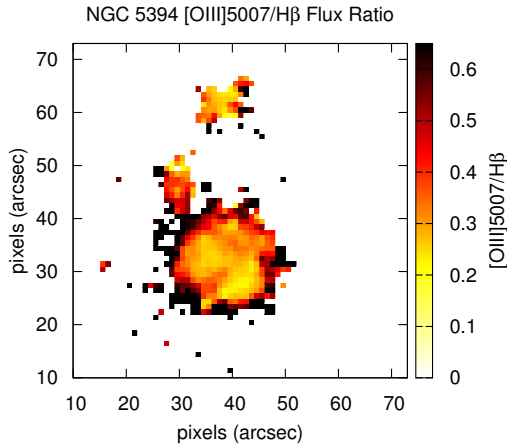


Figure 11. Map of [OIII]5007/H β ratio (O3 index).

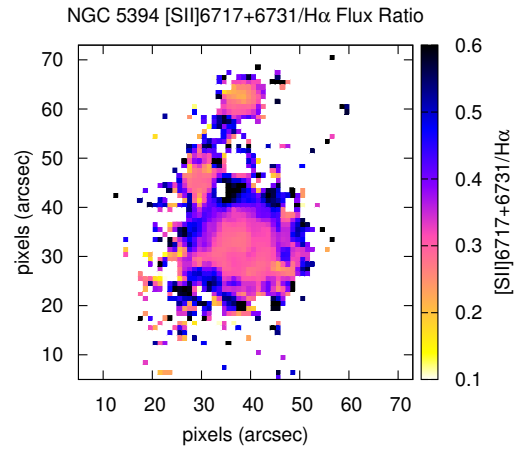


Figure 14. Map of the [SII]6717+6731/H α ratio.

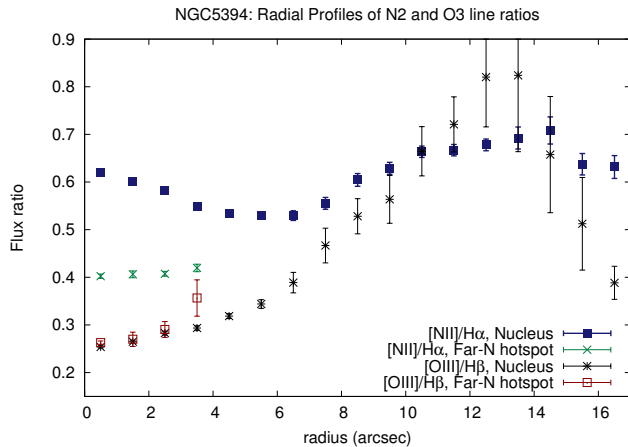


Figure 12. Radial profiles of the line ratios N2 and O3 (centred on the nucleus), and for comparison the profiles centred on the far-N hotspot.

could be explained by high-velocity ($\sim 350 \text{ km s}^{-1}$) shocks with ‘ionized precursor’, from a super wind, an outflow driven by a central starburst. If the nuclear starburst in NGC 5394 causes similar shock ionization, this would appear directly in front of the nucleus due to the face-on orientation. However, at the nucleus, O3 and the other two key ratios [OI]6300/H α and [SII](6717+6731)/H α (Fig 12 to 15) do not show high values or any peak relative to larger radii, and all three (in contrast to the N2 ratio), remain within the range expected for HII regions, and so give no evidence of shocks (or AGN) here.

The flux ratio of the two lines in the [SII] 6717,6731 doublet is a useful diagnostic of electron density (n_e) in nebulae, most sensitive at $n_e \sim 10^2\text{--}10^4 \text{ cm}^{-3}$ (with also a small dependence on temperature, see e.g. Cantó et al. 1980). In NGC 5394, the [SII]6717/6731 ratio (Fig 16 and 17) shows a strong monotonic gradient at $r < 6 \text{ arcsec}$, falling from 1.4 in the outer disk ($r \sim 6\text{--}12 \text{ arcsec}$) to 0.97 at the cen-

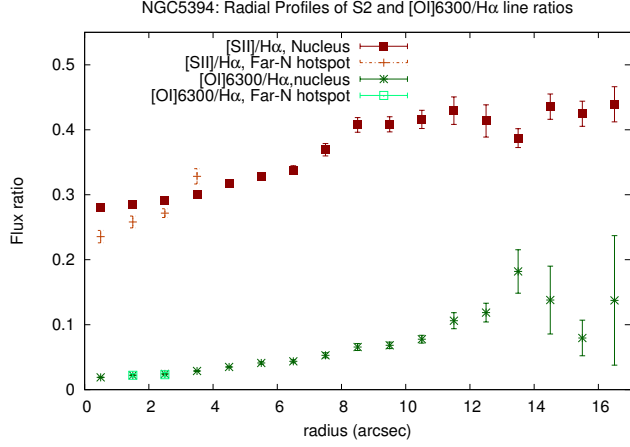


Figure 15. Radial profiles of the line ratios $\text{OI}/\text{H}\alpha$ and $[\text{SII}](6717 + 6731)/\text{H}\alpha$ in the disk, and centred on the far-N hotspot.

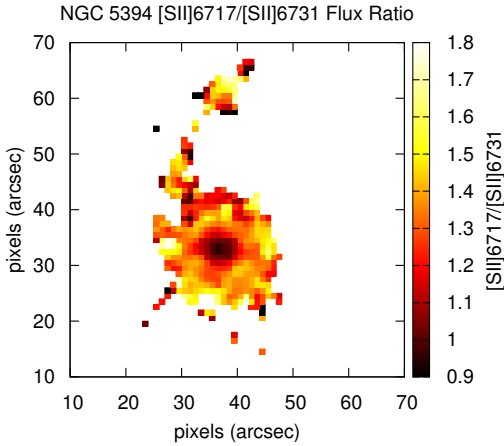


Figure 16. Map of $[\text{SII}](6717)/[\text{SII}](6731)$ ratio, sensitive to electron density n_e

tral 5 and 0.949 in the central one pixel. For the calibration in *iraf.stsdas.nebula.temden*, assuming $T_e = 10000\text{K}$, this signifies a rise in electron density from $n_e \simeq 27\text{ cm}^{-3}$ to a central 750 cm^{-3} . The higher $[\text{SII}](6717/6731)$ ratio of 1.55–1.6 in the far-N hotspot indicates a lower density, probably $n_e \leq 20\text{ cm}^{-3}$. For the galaxy as a whole the integrated $[\text{SII}](6717/6731)$ ratio is 1.191 (corresponding to 252 cm^{-3}).

In NGC 4676, Wild et al. found intermediate $[\text{SII}](6717/6731)$ ratios of 1.1–1.2 ($n_e \simeq 200\text{--}400\text{ cm}^{-3}$) in the bicones and both disks, without obvious radial gradients. The non-interacting M33 spiral, studied with the same PMAS spectrograph (Lopez-Hernandez et al. 2013), does show a gradient from an outlying HII region with $[\text{SII}](6717/6731) \simeq 1.5\text{--}1.8$ (very low n_e), to the nuclear HII region with 1.30 ($n_e \sim 100$), to the very centre with 1.07 ($n_e \simeq 328\text{ cm}^{-3}$). In the starburst-merger Arp 299 (Heckman et al. 1999) n_e similarly increases from ~ 50 to $250\text{--}300\text{ cm}^{-3}$ at the centre. Le Tiran et al. (2011) found the stacked spectra of $z = 1.3\text{--}2.6$ starburst galaxies to indicate mean n_e

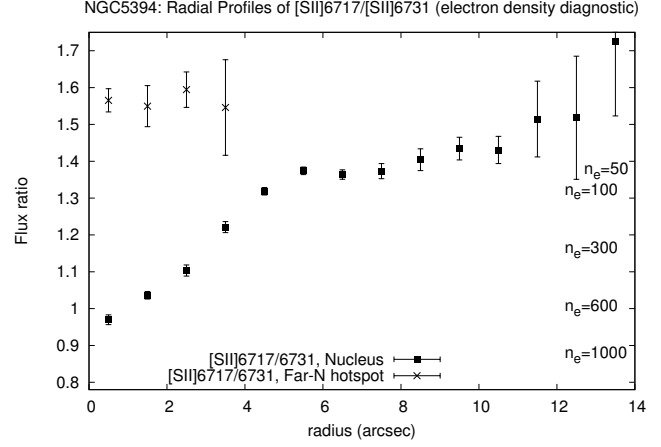


Figure 17. Radial profiles of the line ratios $[\text{SII}](6717)/[\text{SII}](6731)$ in the disk, and centred on the far-N hotspot. An n_e scale is shown for $T_e = 10000\text{K}$.

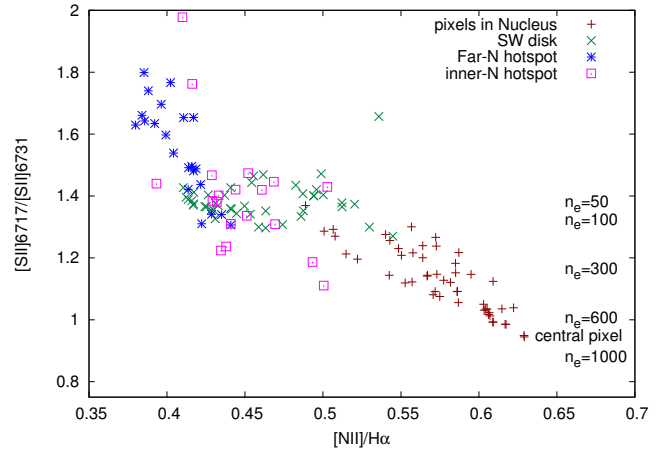


Figure 18. Plot of the line ratios N2 vs. $[\text{SII}](6717)/[\text{SII}](6731)$ in the strongly star-forming regions, showing that they are correlated (the correlation coefficient is 0.8375) forming a sequence of increasing n_e . An n_e scale is shown for $T_e = 10000\text{K}$.

values of 200 cm^{-3} (range $100\text{--}500$) for the $\text{H}\alpha$ -brightest regions, similar to local starbursts. On this basis, the $n_e \sim 750\text{ cm}^{-3}$ in the NGC 5394 nucleus is a fairly extreme case, probably a consequence of the interaction.

Kewley et al. (2013) predict in stellar photoionization models that increasing n_e from 10 to 1000 cm^{-3} could, by increasing collisional excitation, raise the N2 ratio by as much as 0.2 dex (their Fig 2; note that O3 is also increased by a similar amount). This might in itself account for the central high peak of N2 in NGC 5394, even without shocks or AGN. Observationally a high n_e is associated with a positive N2 offset in the BPT diagram for SDSS galaxies (Brinchmann, Pettini and Charlot 2008) and for individual HII regions in CALIFA (Fig 2 of Sánchez et al. 2015). Plotting for the individual pixels in the 4 main star-forming regions (Fig 18), N2 is closely correlated with the $[\text{SII}](6717/6731)$ ratio, which supports n_e as the primary cause of the central enhancement.

In contrast, the outer, annular region of high N2 and other ratios is not associated with any increase in n_e . To

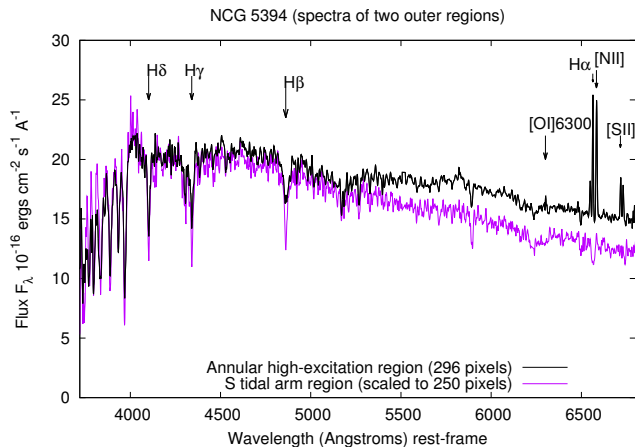


Figure 19. Summed spectrum of the annular high-excitation region where the N2 ratio exceeds 0.65, in total 296 arcsec². Also shown for comparison is the (scaled-up) spectrum from a 14 pixel region of the S tidal tail.

confirm this region is genuine and investigate further we sum the spectra of all 296 pixels at $9 < r < 16$ arcsec with $N2 > 0.65$ to give the spectrum shown in Fig 19. H α and [NII]6584 are well-detected, with a ratio that appears close to unity on the plot, but in the integrated line fluxes from Porto3D H α is corrected upward for stellar absorption and the resulting mean N2 for these pixels (weighted by flux rather than area) is 0.741. In the same way the other mean ratios are found to be [OIII]/H β = 0.844, [SII]/H α = 0.432 and [OI]/H α = 0.060. The [SII]6717/6731 ratio is 1.37, giving a low n_e of 20 cm⁻³. The H α emission and H δ absorption EW are both quite moderate at 4.7Å and 4.1Å so this is neither a starburst or a predominantly post-starburst region.

The elevated line ratios in this region resemble (but are a little more moderate than) the shock-dominated outer regions of the late merger NGC 3256 (Rich et al. 2011), the extensive eastern shock region of the colliding NGC 7318 in Stephan’s Quintet (Rodríguez-Baras et al. 2014) and the bicones in the Mice. All 4 ratios would fit the models of Rich, Kewley and Dopita (2011) for composite shock excitation and HII regions, where the shock component is $\sim 50\%$ (of the H α flux). Further comparison with the models tabulated by Allen et al. (2008) finds a dominant shock component can fit the observed line ratios quite well with shock velocity $v \simeq 225\text{--}275$ km s⁻¹ and little or no pre-ionization (which would give a higher O3); this assumed near solar metallicity, magnetic equipartition ($B = 3.23\mu\text{G}$) and a low electron density $n_e = 1$ cm⁻³.

The total H α flux (uncorrected for dust) from this shock region is 9.4×10^{-15} erg cm⁻²s⁻¹ ($L = 3.2 \times 10^{39}$ erg s⁻¹) only 2.6% that of the whole galaxy, so shocks remain a small (few percent) component of the galaxy’s emission-line luminosity compared to star-formation. Note that this region only appears annular in ratio maps, while all the line fluxes increase towards the centre, so it is possible this emission component extends over the whole disk, but is not apparent inward of $r \sim 4$ kpc where star-formation dominates the H α flux with a lower N2. In e.g., the elliptical NGC 4696, which has shocks from an ongoing merger but very little star for-

mation (Farage et al. 2010), the N2 ratio remains uniformly close to 2.

Similar high line ratios have also been observed in some passive, non-interacting galaxies, e.g. a mean N2 ratio 2.2 in the early-type CALIFA sample of Papaderos et al. (2013), which may be the result of hard continua from post-AGB stars, planetary nebulae or ‘hot low mass evolved stars’, but in these cases the lines are fainter, with $EW \leq 2\text{Å}$. Fig 19 shows for comparison a scaled-up spectrum from a region in the southern tidal tail (also on Fig 4). The spectra are quite similar except the tail is a little bluer (less dust?), has stronger Balmer absorption, but lacks the emission lines (there is possibly a weak [NII] line but the EW is no more than 0.8Å). This is the part of the galaxy most dominated by the intermediate age stellar population. These stars cannot be making more than a very small contribution to the high excitation region, and we look elsewhere for the power source (see section 6.3).

5 METALLICITY GRADIENTS AND THE BPT DIAGRAM

Metallicities of galaxies or sub-regions can be estimated by a great variety of methods. One of the simplest requires only O3 and N2 ratios to estimate the nebula gas metallicity, and can be applied even to high redshifts, with dust having little effect, but these ratios are subject to other influences (especially AGN) and there are uncertainties in calibration. The O3N2 index, given as $\log_{10}[\text{O3}/\text{N2}]$, is -0.387 at the centre of NGC 5394 and -0.184 for the galaxy as a whole. In the widely used PP04 (Pettini and Pagel 2004) calibration, metallicity expressed as the logarithmic ratio of oxygen to hydrogen, $12 + \log(\text{O}/\text{H}) = 8.73 - 0.32 \times \text{O3N2}$. Marino et al. (2013), comparing line ratios from the CALIFA survey with calibrations based on electron temperature, derived a shallower relation, $12 + \log(\text{O}/\text{H}) = 8.533 - 0.214 \times \text{O3N2}$.

A different metallicity measure is obtained from the stellar component. Stellar and nebular metallicity may differ, as stars preserve a record of the abundances at the time of their formation, which may be Gyr ago, and gas may move in or out. Porto3D model fitting generated maps of luminosity-weighted and mass-weighted stellar metallicity (lwZ and mwZ), the former giving more weight to recently formed stars, in units of Z (total mass fraction of $N_{\text{atomic}} \geq 3$ elements), which are here converted to O/H on the basis that solar metallicity is $Z = 0.015$ and $12 + \log(\text{O}/\text{H}) = 8.72$ (Allende Prieto et al. 2001). Fig 20 shows the O3N2 nebular metallicity averaged in radial annuli, using only pixels with $F(\text{H}\alpha) > 10^{-16}$ and signal/noise > 3 for both ratios (so there is a gap between the disk and the N hotspot). Pixels with $N2 > 0.7$ or O3 > 0.7 are also excluded on the basis that they are likely to be more dominated by shocks than by star-formation, but this has little effect on the mean O3N2 values (shocks might cause O/H to be underestimated by increasing the O3 ratio but this may largely be compensated by the increase in N2). Fig 20 also shows the stellar lwZ and mwZ in the same annuli (using all pixels).

The PP04 calibration gives a much higher metallicity than Marino et al. (2013), $12 + \log(\text{O}/\text{H}) \simeq 8.79/8.85$ integrated/central ($1.17\text{--}1.35Z_{\odot}$), compared to $8.57/8.62$ ($0.71\text{--}0.79Z_{\odot}$). The latter is much closer to the model-fit stellar

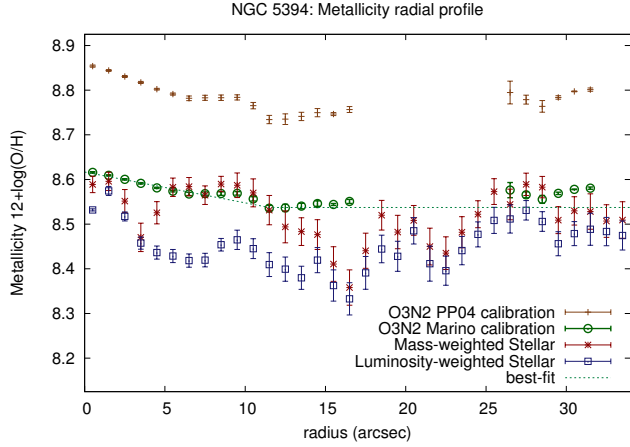


Figure 20. Radial profiles of the nebular (O3N2) metallicities with PP04 and Marino et al. (2013) calibrations (with our fitted gradient), and of the luminosity-weighted and mass-weighted stellar metallicities from the Porto3D fits.

mwZ. From $r = 0.5$ to $r = 11.5$ arcsec the Marino et al. O3N2 metallicity decreases by 0.080 ± 0.006 dex, but beyond this remains flat (perhaps even increasing slightly in the outer hotspot). A linear fit at $r < 12$ arcsec gives $8.6166 - 0.0069(\pm 0.0002)r$ (plotted on Fig 20), and for $r < 8$ arcsec only, $8.6205 - 0.0083(\pm 0.0003)r$. These gradients are -0.028 and -0.033 dex/kpc, or with the disk exponential scale $h = 6.5$ arcsec (Puerari et al 2005) corresponding to $r_{eff} = 10.9$ arcsec (2.75 kpc), can also be expressed as -0.076 and -0.091 dex/ r_{eff} .

Sánchez et al. (2014) found CALIFA disk galaxies typically had a metallicity gradient of -0.1 dex/ r_{eff} at $0.3 < r < 2 r_{eff}$, with flattening at even larger radii and evidence of a shallower mean gradient (-0.05) for interacting than for non-interacting (-0.11) subsamples (these estimates used the PP04 calibration and would be reduced by $1/3$ for that of Marino et al.). Rich et al. (2012) found similar gradients, which flattened as mergers progressed. NGC 5394 appears consistent with their mean for early-stage mergers, but also with the non-interacting disks of the same mass in Ho et al. (2015). Simulations predict that interactions reduce the central O/H and flatten gradients by the infall of low-metallicity gas (Rupke, Kewley and Barnes 2010), but there is also a competing effect of re-enrichment by star-formation (Torrey et al. 2012), so the resulting evolution is more complex (in disk galaxies with high gas fractions the central O/H may even be increased).

A new study by Barrera-Ballesteros et al. (2015), comparing interacting and isolated disk galaxies in CALIFA, suggests that the effect of interactions on O/H is more complex than a simple progressive flattening. They found interactions had little effect on the average central O/H, and might even steepen metallicity gradients at small radii ($r < 0.5 r_{eff}$) where interacting galaxies show an enhancement in SFR. At larger radii ($r \sim 1-2 r_{eff}$) the mean metallicity is reduced and it must be here the gradient is flattened. This was attributed to the inflow of lower metallicity gas. Also gradients in the outer galaxy could be ‘stretched’ out by the formation of tidal tails (Rich et al. 2012). These pro-

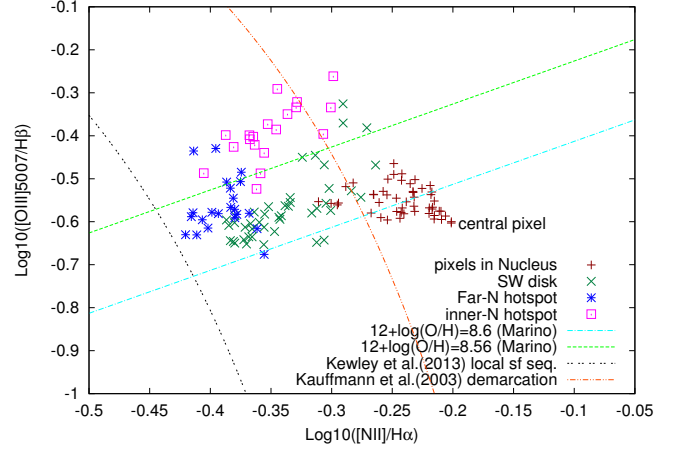


Figure 21. ‘BPT’ diagram plot of the log of O3 vs. N2, for the pixels in the regions of strong star-formation, showing the local star-forming sequence from Kewley et al. (2013), the HII/composite demarcation of Kauffmann et al. (2003) and two iso-metallicity lines based on the Marino et al. (2013) calibration.

cesses could explain NGC 5394 having a ‘normal’ O/H gradient at $r < 10$ arcsec which becomes flat only at $r > r_{eff}$.

The mwZ shows no significant gradient in the disk (from $r = 0$ to $r = 8.5$ arcsec changing by -0.0018 ± 0.0331), whereas the lwZ falls steeply (-0.1135 ± 0.0151 between $r = 0.5$ and $r = 6.5$), and remains much lower than the mwZ in the outer disk, e.g. by 0.1359 ± 0.0222 at $r = 8.5$ (a 6σ difference). This is surprising in view of the expectation that metallicity would increase with time, which would give $lwZ > mwZ$. Again a possible explanation is that the intermediate age and recent starbursts were fuelled by inflowing gas of lower metallicity compared to the underlying older disk stars, and, as Fig 8 of Barrera-Ballesteros et al. (2015) suggests, the resulting O/H reduction is most apparent not at the centre but at $r \sim 5-10$ arcsec ($0.5-1 r_{eff}$).

Returning to the nebular metallicity, Fig 21 shows the BPT (Baldwin, Phillips and Terlevich 1981) diagram, i.e. log O3 vs. log N2, for the principal star-forming regions, together with two isometallicity lines (using the Marino et al. calibration), and the ‘local star-forming sequence’ from Kewley et al. (2013), which is obtained from a photoionization model (with low electron density) and fits the locus of typical $z < 0.1$ star-forming galaxies in the SDSS. The latter is essentially a sequence of increasing metallicity (right/downwards) and approximately orthogonal to the isometallicity lines (on which $\Delta(\log N2) \simeq \Delta(\log O3)$). The distribution of CALIFA pixels shows the increase in metallicity from the outer star-forming regions to the central pixel, but combined with this, a large shift in the orthogonal direction, along the isometallicity lines and away from the local sequence, by as much as 0.2 dex in N2. This latter cannot be due to metallicity but is as expected for a steep increase in n_e towards the centre (Kewley et al. 2013) and we propose this is the cause. The entire nuclear region transgresses the Kauffmann et al. (2003) demarcation, which was intended to divide pure star-forming galaxies from HII/AGN composites, but is too conservative in not fully allowing for the potential [NII] enhancement of high n_e and hard radiation

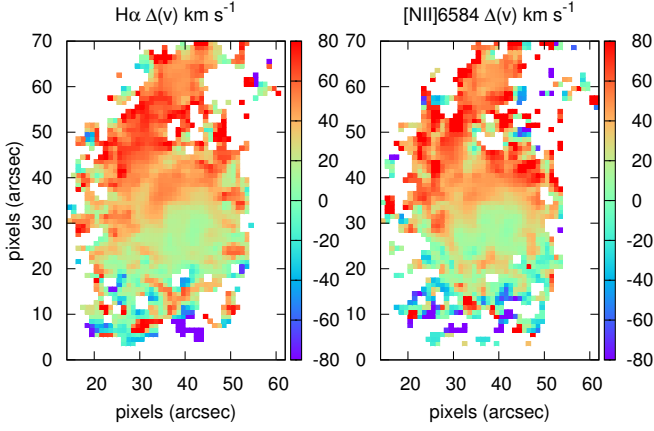


Figure 22. Maps of the line-of-sight relative velocity $\Delta(v)$, from the red/blue-shifting of the emission lines H α (left) and [NII]6584 (pixels shown white, which have little emission, do not have valid measurements). Note they are closely similar.

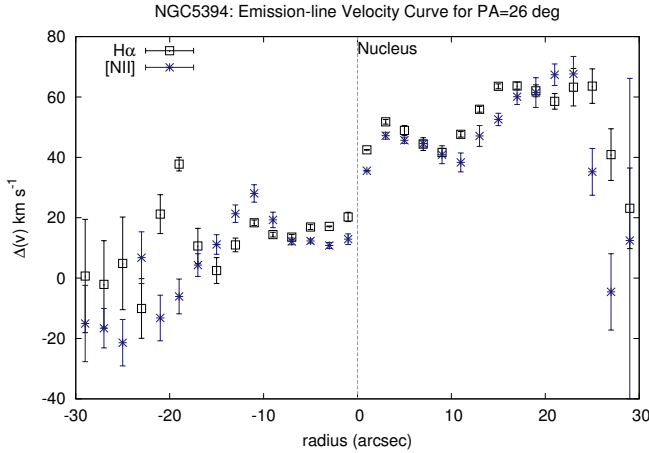


Figure 23. Line-of-sight velocity curve from the H α wavelength averaged in $\pm 15^\circ$ sectors on the kinematically determined axis, position angle $\phi_k = 26^\circ$ (East of North), with the NNE direction denoted positive.

fields, which can move HII regions across the line (e.g. Fig 2 of Sánchez et al. 2015).

6 KINEMATICS

6.1 Rotation of the Disk

Fig 22 shows a map of the line-of-sight velocity as measured from the H α line, and also for [NII]6584. The galaxy is inclined only 15° from face-on, according to K02, so that the line-of-sight $\Delta(v)$ is lower than the true rotation of the disk by a factor 3.9. Even so, the velocity gradient from rotation is clearly visible in the H α velocity map. We obtain a velocity curve $v_{rot}(r)$ by averaging this map in two opposite sectors centred on the nucleus, in 2-arcsec bins of radius and within position angles $\theta = \phi_k \pm 15^\circ$ and $\theta = (\phi_k + \pi) \pm 15^\circ$ where ϕ_k

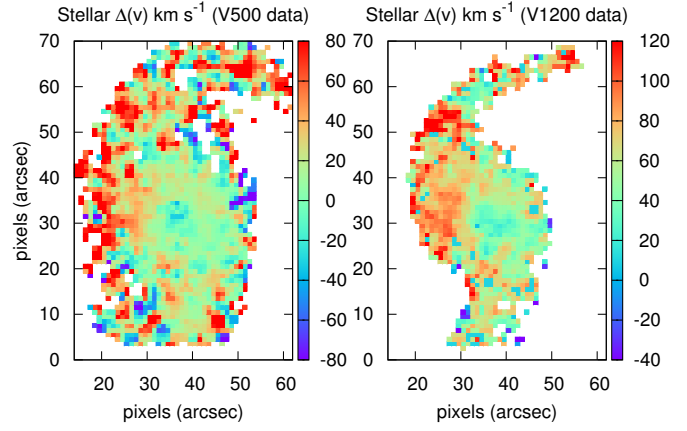


Figure 24. Map of the stellar line-of-sight relative velocity $\Delta(v)$ measured by fitting to the spectra (i.e. from absorption lines) on the V500 and the V1200 data.

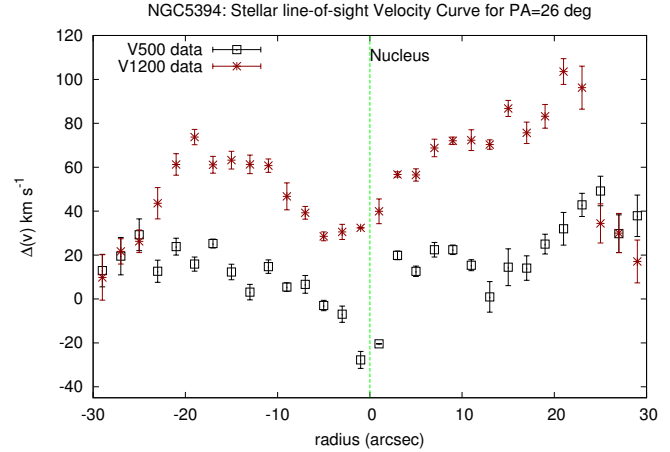


Figure 25. Line-of-sight velocity curve from the stellar spectra, shown for both the V500 and V1200 data averaged in $\pm 15^\circ$ sectors on the position angle $\phi_k = 26^\circ$.

is the kinematic position angle of the galaxy. The velocity curve is evaluated in this way for all PAs ϕ and we and ϕ_k estimated as the angle which maximises the velocity difference between the opposite sides, i.e. $\Sigma_{r=0}^{r=22''} [v_{rot}(r) - v_{rot}(-r)]$; this gave $\phi_k = 26 \pm 13^\circ$, in agreement with the kinematic (receding side) PA of 25.8° measured for this galaxy by García-Lorenzo et al. (2015).

We take ϕ_k as 26° and Fig 23 shows the H α $v_{rot}(r)$ along this axis (NNE is positive, SSW is negative). The velocity curve shows the gradient produced by the galaxy's rotation, with an amplitude (taken as half the difference between the mean of the two largest velocity measurements on each side) 35 km s^{-1} . It is relatively symmetric, but with minima on both sides at $r \simeq 10 \text{ arcsec}$ followed by steeper gradients, a feature seen in some barred galaxies and which might correspond to the weak distortion K99 found in the H α velocity map some 8 arcsec NE of the nucleus. The [NII] velocity curve is very similar and gives an amplitude 43 km s^{-1} . The

disk rotation velocity must be at least $\sim 40 \times 3.9 = 156 \text{ km s}^{-1}$, which is typical for a spiral galaxy in this stellar mass range ($\sim 2.4\text{--}4.6 \times 10^{10} M_{\odot}$), e.g. Cortese et al. (2014).

Shocks and ionized outflows are associated with mergers (Rich, Kewley and Dopita 2011, 2014), and might be revealed by kinematics, e.g. Yuan et al. (2013) attributed a high-N2 region to shocks/outflows as it was $\sim 100 \text{ km s}^{-1}$ blueshifted with respect to the galaxy. The $\Delta(v)$ map for [NII]6584 might be more sensitive to shocks than H α . However, the two velocity maps are very similar, and neither shows any region of blueshifted emission (ionized outflowing gas), either at the nucleus or in the outer (annular) high-N2 region.

Fig 24 shows the stellar $\Delta(v)$ maps, obtained by fitting the emission-subtracted spectra with Starlight stellar models, for both the V500 data and the higher-resolution V1200, and Fig 25 the stellar velocity curves measured in the same way on the PA $\phi_k = 26^\circ$, centring on the nucleus in each case. The stellar $\Delta(v)$ maps, especially from V500, show a localized blueshift ($\sim 20 \text{ km s}^{-1}$) near $r \simeq 0$ and the cause is discussed below. The V500 stellar velocities show a weaker velocity gradient, with an amplitude (excluding the centre) only 21 km s^{-1} , but those from the V1200 data have a stronger gradient and a positive offset with maximum amplitude 49 km s^{-1} . Cortese et al. (2014) found that stellar rotation velocities in SAMI disk galaxies averaged $0.14 (\pm 0.11)$ dex lower than v_{rot} from nebular emission lines, but considering the large uncertainties and low inclination it is not clear if the two differ significantly in this galaxy.

6.2 Evidence of an Outflow

We did not see evidence of outflowing ionized gas in the H α and [NII] velocity maps. Also both line profiles appear quite symmetric (although asymmetry was reported by K99), at least at the resolution of the V500 data, and are well-fitted by Gaussians. Any blueshifted line emission must be very faint compared with the star formation in the disk. However, the cool gas phase of outflows may instead show itself in absorption lines, in particular MgII(2796,2803) and NaI (5890,5896). The nuclear spectrum plotted in Fig 4 has a very strong absorption line at 5890 \AA restframe, which can be identified as the NaI (5890,5896) doublet, unresolved by the V500 grating and slightly blueshifted. While this line appears in purely stellar spectra (especially from K type stars), a stronger and blueshifted NaI absorption, seen in many LIRGs/ULIRGs (e.g. Heckman et al. 2000), is a signature of starburst-driven outflows.

To investigate this we sum the stellar model fitted by Porto3D over the same 5 pixels of the nucleus and compare this with the observed spectrum (Fig 26). The NaI line observed here with $\lambda = 5889.62 \pm 0.09 \text{ \AA}$ and $\text{EW} = 7.03 \pm 0.06$ is > 3 times stronger than, and blueshifted with respect to, the purely stellar model where the blended doublet is fitted by a Gaussian with $\lambda = 5892.73 \pm 0.24 \text{ \AA}$ with $\text{EW} = 2.26 \pm 0.07 \text{ \AA}$. The observed line blueshift is $3.11 \pm 0.26 \text{ \AA}$ or $158 \pm 13 \text{ km s}^{-1}$. Taking the (observed-model) residual spectrum isolates the non-stellar, interstellar-gas component of the NaI line, which is here $\lambda = 5888.45 \pm 0.09 \text{ \AA}$, and by comparison with the (Starlight-model) stellar NaI gives the blueshift of the non-stellar component as $4.38 \pm 0.26 \text{ \AA}$ or $223 \pm 13 \text{ km s}^{-1}$.

This is indicative of a neutral gas outflow from the nucleus, directed perpendicular to the disk. In Fig 7, the spectrum of the nucleus region, integrated over 50 pixels ($r < 4 \text{ arcsec}$), shows enhanced NaI absorption with $\text{EW} = 5.52 \pm 0.02 \text{ \AA}$ at $\lambda = 5890.12 \pm 0.02 \text{ \AA}$ (almost as strong as for the central 5 pixels only), but elsewhere the NaI line is consistent with the stellar models in EW (only $1\text{--}2.5 \text{ \AA}$) and $\lambda (\simeq 5892\text{--}3 \text{ \AA})$. This confirms the strong blueshifted absorption originates in the galaxy centre and is not a spurious feature produced by sky lines or some instrument problem. The outflow appears to have a similar, but weaker effect on the CaII ‘K’ absorption line at 3933 \AA ; in the central 5 pixels the observed and stellar model wavelengths are measured as 3931.48 \AA (EW 3.6 \AA), 3933.04 \AA (EW 2.0 \AA), and the residual (excess absorption) is at 3930.30 \AA , which corresponds to a very similar outflow blueshift $\Delta(v) = -209 \text{ km s}^{-1}$. This outflow might also explain the stellar velocity maps appearing slightly blueshifted at the centre. These $\Delta(v)$, measured by cross-correlation, could have been locally biased (up to $\sim 20 \text{ km s}^{-1}$ blueward) by the effect of the outflow on some absorption lines, especially in the V500 spectra which contain the NaI doublet.

We calculate (integrating over wavelength) a map of the NaI EW (Fig 27); the regions of excess absorption approximately fills the central $r < 4 \text{ arcsec}$ ($r < 1 \text{ kpc}$) and, measuring with IRAF ellipse, has a FWHM $6.4\text{--}7.0 \text{ arcsec}$ (much larger than the instrumental FWHM of 3.5 arcsec) and in the outer isophotes is slightly extended to the SE (at the $\text{EW} = 3.5 \text{ \AA}$ isophote, $\text{PA} = -36 \pm 3 \text{ deg}$ and ellipticity $= 0.24 \pm 0.02$; using IRAF ellipse). Alongside we show a $\Delta(v)$ map obtained by Gaussian-fitting the NaI absorption in each pixel (with IRAF fitprof, over 5879 to 5920 \AA , avoiding the weak HeI emission line at 5876 \AA). The blueshifted and high-EW regions correspond spatially, being extended by $> 1.5 \text{ kpc}$ on a PA close to the inner-disk minor axis, which seems consistent with an outflow perpendicular to the disk. Over this central region the total flux absorbed in the residual (non-stellar i.e. outflow) line is $1.44 \times 10^{-14} \text{ erg cm}^{-2} \text{ s}^{-1}$.

The EW and $\Delta(v)$ of the NaI absorption are comparable to the NaI lines in many of the starbursting, $L_{\text{IR}} = 10^{10\text{--}12} L_{\odot}$ galaxies in Heckman et al. (2000), which have dust-rich super-winds. Blueshifted NaI absorption is observed to a lesser degree in more typical disk galaxies (Chen et al. 2010); the detection probability increases with central SFR, face-on orientation and high dust reddening, and the correlation of $\Delta(v)$ with disk orientation implies the outflows are perpendicular and entrained within bicones of opening angles ≤ 60 degrees (Wild et al. 2014 measured this angle directly for NGC 4676A as $\Omega_w/4\pi = 0.37$, corresponding to 51°). The NaI blueshift/outflow velocity is also correlated with SFR, with $\sim 200 \text{ km s}^{-1}$ for $10 M_{\odot} \text{ yr}^{-1}$, and Bordoloi et al. (2014) found the same correlations for $z \sim 1$ galaxy outflows observed in MgII 2796,2803. Our $\Delta(v)$ is slightly above average for the SFR but within the typical range.

Heckman et al. (2000) give a formula (eq 5) for estimating outflow rate as $dM/dt \sim 60(r_*/\text{kpc})(N_H/3 \times 10^{21} \text{ cm}^{-2}) \times (\Delta v/200 \text{ km s}^{-1}) \times (\Omega_w/4\pi) M_{\odot} \text{ yr}^{-1}$. Putting in starburst radius $r_* = 0.75 \text{ kpc}$, $N_H = 6.1 \times 10^{20}$ at the centre (from Fig 5 of K02), $\Delta v = 223 \text{ km s}^{-1}$ and $\Omega_w/4\pi \simeq 0.37$, gives $dM/dt \simeq 3.77 M_{\odot} \text{ yr}^{-1}$, similar to our estimate for the SFR. Heckman et al. (2000) (and similarly Bordoloi et al. 2014)

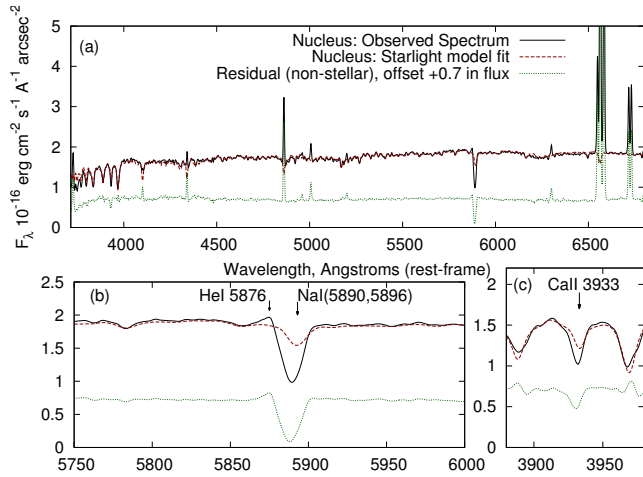


Figure 26. Observed spectrum of the central 5 pixels compared with the Starlight stellar model fit, for (a) the whole spectrum and (b) for the region of the NaI(5890,5896) absorption doublet, together with the observed - model residual, showing that there is substantial blueshifted, non-stellar NaI absorption at the central region of NGC 5394. (c) This blueshifted absorption may also be visible, less strongly, in the CaII (K) line at 3933Å.

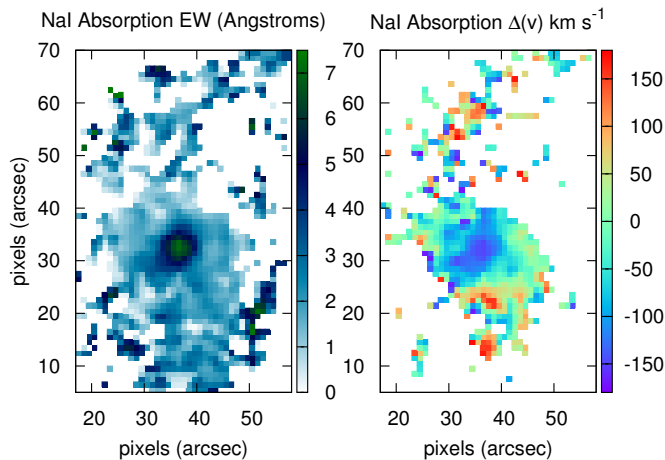


Figure 27. (a) Map of the equivalent width of the NaI(5890,5896) absorption doublet, obtained by integrating over the line (5879–5904Å), clearly showing the central region of strong absorption (up to $EW = 7\text{Å}$), in excess of that expected for stars alone (about 2Å); (b) map of the velocity shift $\Delta(v)$ of the NaI absorption line relative to the stellar-fit 5892.73Å , as obtained by a Gaussian fit to each pixel over 5879–5920Å.

concluded that typically a ‘superwind is expelling matter at a rate comparable to the star formation rate’. The kinetic power would be $\frac{1}{2} \frac{dM}{dt} v^2 = 5.9 \times 10^{40} \text{ erg s}^{-1}$; 1/13 the galaxy’s dust-corrected $H\alpha$ luminosity (Table 1).

6.3 ... and Infall?

The outer high-excitation region (at $9 < r < 16 \text{ arcsec}$) does not show the same blueshifted $\Delta(v)$ as the outflow from the nucleus. Although very apparent in line ratio maps it seems

to leave no imprint on the velocity maps in either $H\alpha$ or [NII], suggesting little motion perpendicular to the disk of the underlying galaxy. Nor is it associated with a significant broadening of the [NII] line (at least at this resolution), which remains at $FWHM \simeq 6\text{Å}$ across the galaxy. This may be similar to the late-stage merger NGC 3256, in which the outer regions with high, shock-like line ratios are blueshifted only ‘a few 10 km s^{-1} ’ (Rich et al. 2011), whereas the central strong NaI absorption (caused by outflow) is blueshifted by $\Delta(v) = -309 \text{ km s}^{-1}$ (Heckman et al. 2000).

The non-visibility of the outer high-excitation region in $\Delta(v)$ maps would argue that it is not outflowing gas driven by the nuclear starburst. We suggest that the starburst-driven outflow remains collimated in front of the central disk, as on the NaI map (Fig 27), and the outer high excitation region is powered instead by the kinetic energy of gas spiralling inwards within the disk plane, where it would have little $\Delta(v)$ in the line-of-sight direction, as a result of tidal forces from the interaction. The gas would lose angular momentum in the shocks and eventually form stars.

This mechanism was argued for the outer regions of high excitation/line ratios found in a number of interacting or merging luminous infra-red galaxies (Monreal-Ibero et al. 2010, Rich et al. 2011). One argument was that the occurrence of outer high-excitation regions was more correlated with (late) interaction stages than with high SFR. In the Torrey et al. (2012) merger simulations for a similar mass galaxy, the nuclear gas inflow rate is generally $\sim 0.5\text{--}1.0 \times \text{SFR}$ and $1\text{--}5 \text{ M}_{\odot} \text{ yr}^{-1}$. At the velocities of disk rotation $\sim 160\text{--}170 \text{ km s}^{-1}$ or as estimated for the shocks, $\sim 250 \text{ km s}^{-1}$, and an inflow rate of at a few $\text{M}_{\odot} \text{ yr}^{-1}$, the kinetic energy input would be sufficient to power the shock component of line emission ($\sim 10^{40} \text{ erg s}^{-1}$).

7 HISTORY OF THE INTERACTION

NGC 5394 is now undergoing a nuclear starburst (generating an outflow), has other localized knots of star-formation, and shows evidence of a more extensive (over most of the galaxy) episode of star-formation 10^8 to 10^9 years ago. Fig 28 shows the the Porto3D model-fits mass distributions of young ($< 100 \text{ Myr}$) and intermediate age ($0.1\text{--}1.0 \text{ Gyr}$) stars. The young population has a total mass 206 million M_{\odot} and is very centrally concentrated with 132 million M_{\odot} in the central $< 4 \text{ arcsec}$ and only 1.7 million in the far-N hotspot. The dust-corrected $H\alpha$ SFR in Table 1, especially if further corrected to the Salpeter IMF of these masses (giving $6 \text{ M}_{\odot} \text{ yr}^{-1}$) implies the current SFR is significantly higher than the mean ($2.06 \text{ M}_{\odot} \text{ yr}^{-1}$) for the past 10^8 yr . Similarly our SFR of 3.39 M_{\odot} is more than twice the $1.54 \text{ M}_{\odot} \text{ yr}^{-1}$ estimate of Lanz et al. (2013) based on SED-fitting with a model of the same IMF and 100 Myr of constant star-formation. $H\alpha$ traces only the very recent SFR ($\leq 10 \text{ Myr}$), compared to longer timescales for the infra-red emission, so the implication is again the SFR has increased strongly over the past 10^8 yr .

The intermediate-age population has a very different distribution, in the outer disk as a broad ring and, especially, throughout the outer tidal arms. The earlier starburst must have been spread over the whole galaxy, whatever its shape at that time. The total mass of intermediate

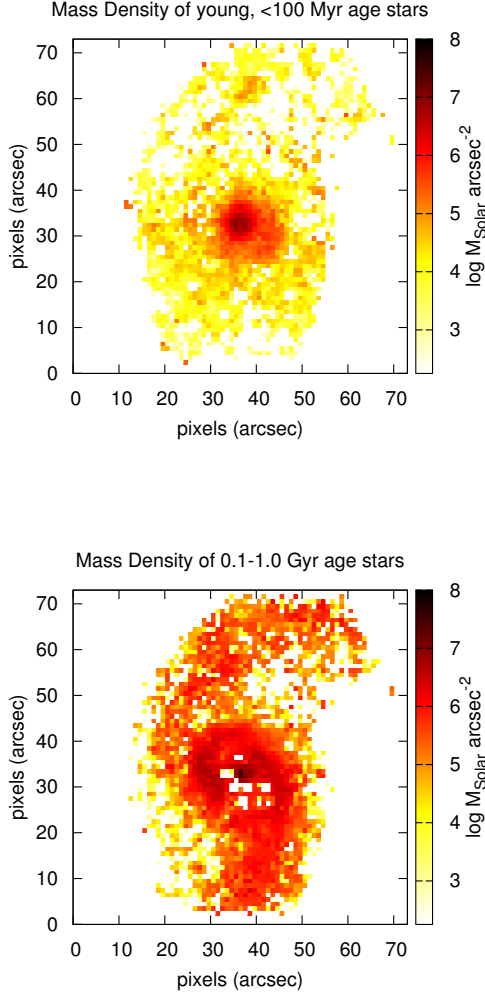


Figure 28. Distribution of the young (age zero to 100 Myr) and intermediate age stellar population (age 100 Myr to 1 Gyr), as estimated from the Starlight model fits, shown on a log scale of stellar mass per pixel.

age stars is estimated as $1.200 \times 10^9 M_\odot$ with only 170 million M_\odot at $r < 4$ arcsec. These patterns recall the merger simulation of Renaud, Bournaud and Duc (2015), in which early star-formation is extensive but the final burst is ‘almost exclusively central, due to gas inflows’. The concentration of star-formation in the SW disk (the inner western arm, see K02), reflects the lopsided distribution of H_2 which would be a short-term effect of the interaction, so is seen in the young population map but not for the intermediate-age stars, which instead are concentrated in the other two disk arms (eastern and outer-western). This agrees with to the ‘west-vs-east time lag’ in star- and arm-formation (K99), with only the inner-western ‘third arm’ that is delayed i.e. recent. Similarly the two hotspots are not seen in the intermediate-age map, as they are younger features.

K99/K02 describe NGC 5394 as ‘post-ocular’ and similar to the interacting galaxy IC 2163 but at a later stage of evolution, with star-formation more concentrated in the

nucleus. IC 2163 is interacting with the larger spiral NGC 2207 and indeed appears eye-shaped with most of its star-formation in numerous hotspots forming two arcs around the rim of the ‘eye’ (Kaufman et al. 2012). In the Struck et al. (2005) simulation of this pair there was a major starburst at the first close passage, some 280 Myr earlier, and there is predicted to be a second burst at least 100 Myr in the future as the galaxies finally merge. NGC 5394 could be 50–100 Myr ahead of IC 2163 and entering this stage, with the SFR increasing again as the galaxy approaches merger. In this simulation the long tidal arms are drawn out of the initially round galaxy very soon after the first close encounter and starburst, and this might account for the tidal arms in NGC 5394 having the highest content of intermediate-age stars.

The Arp 84 system is certainly at a later evolutionary/merger stage than the Mice, for which the simulations of Wild et al. (2014) put the first perigalacticon only 170 Myr ago, and observationally the oldest star clusters in both galaxies date from exactly that time (Chien et al. 2007). The Mice have less $H\delta$ absorption and much less of an intermediate age population than NGC 5394, and in the simulations of Wild et al. (2014) and Barnes (2004) their biggest starburst lies 0.4–0.8 Gyr in the future when the galaxies will merge and the SFR peak at $40\text{--}50 M_\odot \text{yr}^{-1}$.

The hotspots in the northern arm of NGC 5394 are examples of the ‘hinge clumps’ seen in many interacting galaxies (Smith et al. 2014) – bright knots of active star-formation, typically found where tidal arms/tails join to the disk, with $EW(H\alpha) \sim 100 \text{ \AA}$ and $L(H\alpha) \sim 10^{40} \text{ erg s}^{-1}$. Analytical and numerical models of tidal disturbance (Struck and Smith 2012, SS12) can explain many of the galaxy’s features including the formation of long, curved and paired tidal arms (which can extend to ~ 3 times the radius of the pre-interaction galaxy) and an inner disk with a structure described as ocular with internal arms (e.g. Figs 7 and 10 of SS12); furthermore the model predicts ‘swallowtail caustics’ at the base of the tidal tails or arms where intersecting streams of gas would pile up, giving rise to localised star-formation which could be quite sustained and produce ‘hinge clumps’ such as the inner-N hotspot. A refinement of the SS12 model, where a prograde encounter is represented by successive impulses, can produce additional swallowtail caustics far out from the disk on the spiral arms (Fig 12 of SS12) and in this way account for the formation and position of the far-North hotspot (and the similar feature in Arp 82). Introducing a little asymmetry further improves the resemblance to real Arp (1966) galaxies. The high-resolution simulation of Renaud et al. (2015) also predicts the formation of a ‘young massive cluster’ far out on the northern tidal arm. Probably these hotspots will become globular clusters.

In a further attempt to reconstruct the star-formation history we run Starlight model fits on the 7 region spectra (Fig 7), with a set of Chabrier-IMF stellar templates representing 23 ages from 1 Myr to 13 Gyr and four metallicities ($Z=0.004, 0.008, 0.02, 0.05$). For each $f_\lambda(\text{age}, Z)$ template spectrum the program fits the mass of stars present now and at formation. As the results are rather noisy, mean SFRs are estimated for wide $\Delta(\log[\text{age}]) = 0.3$ bins, by summing in each the (at-formation) masses of stars formed, and dividing by the bin width in years. In this model the current stellar mass is only $2.44 \times 10^{10} M_\odot$, reflecting the ‘lightweight’ IMF.

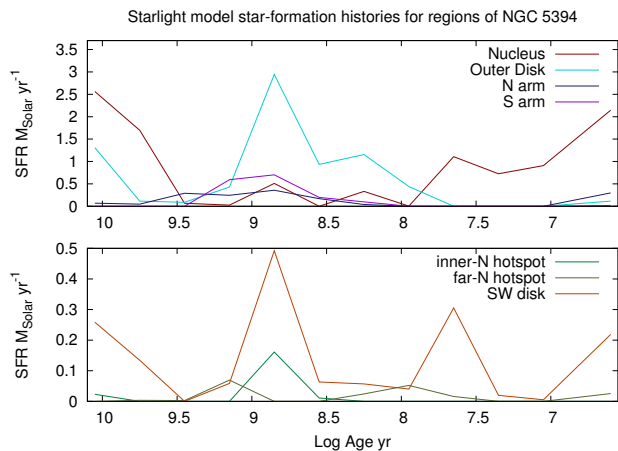


Figure 29. Reconstructed SFR history, estimated from the Starburst model fits, of large (above) and small (below) regions of NGC 5394 as a function of look-back time, plotted in $\Delta(\log[\text{age}]) = 0.3$ intervals.

The model also fits dust extinction to the stellar continuum, $A_v = 1.06$ mag for the nuclear region (notably less than the emission-line $A_{H\alpha} = 2.32$ mag from the Balmer decrement), and $A_v = 0.60$ and 0.31 for the SW and outer disk.

Fig 29 shows the resulting SFR histories. The nucleus has a large old (~ 10 Gyr) stellar population, plus resurgent star-formation (note increasing SFR) over the past 100 Myr. The outer disk and tidal arms are dominated by intermediate age (10^9 – 10^8 yr old) stars, the $H\alpha$ -bright SW disk region has additional star-formation at age < 100 Myr, the star-formation in the far-N hotspot also goes back some 100 Myr, while the inner-N hotspot, with stronger Balmer absorption, is mostly intermediate-age. The model fitted a large component of ~ 0.9 Gyr age stars for the outer disk and tidal arms, suggesting the interaction with NGC 5395 and enhanced star-formation have been going on for a long time, perhaps even with two previous close passages.

The first perigalacticon could have triggered a prolonged influx of gas towards the nucleus, fuelling the subsequent star-formation. If this gas was relatively low metallicity, the stellar metallicity would then decrease during the interaction, which (we argued in Section 5) could account for the (model-fit) luminosity-weighted stellar metallicity being lower than the mass-weighted (Fig 20). Yet this influx did not flatten the O3N2-metallicity gradient at $r \leq 10$ arcsec, perhaps because of competing re-enrichment by star-formation (Torrey et al. 2012). Also O3N2 could be less sensitive to mixing of low-Z gas if prolonged star-formation and reprocessing produced a high central N/O ratio (e.g. Belfiore et al. 2015). Tidally-induced gas infall may be the cause and the energy source of the relatively faint (a few percent of the total line emission) but extensive (~ 8 kpc diameter) outer ring of elevated N2, O3, [OI]/ $H\alpha$ and [SII]/ $H\alpha$ ratios, which are consistent with shocks (of velocity ~ 250 km s $^{-1}$). Extensive shock emission features similar to this have been found in other late-stage or strongly interacting, gas-rich galaxies (Monreal-Ibero et al. 2010, Rich et al. 2011, 2014; Rodríguez-Baras et al. 2014).

We also find evidence for a nuclear-starburst-driven outflow of gas with (blueshift) velocity 223 ± 13 km s $^{-1}$, and estimated the rate as ~ 3.77 M $_{\odot}$ yr $^{-1}$, which from Heckman

et al. (2000) might not be exceptional if the SFR is near our estimate of 3.39 M $_{\odot}$ yr $^{-1}$. Wild et al. (2014) estimated 8 – 20 M $_{\odot}$ yr $^{-1}$ at 350 km s $^{-1}$ for the ionized outflow from NGC 4676A. That the outflow in NGC 5394 is seen as absorption in the neutral line Na I, rather than in emission, might be a feature of the later evolutionary stage, with the neutral outflow persisting longer, as suggested by the detection of neutral outflows in some dusty, red post-starburst galaxies (e.g. Sato et al. 2009), and in recent gas-rich mergers (e.g. NGC 34 in Schweizer and Seitzer 2007). Much higher spectral resolutions ($R \geq 5000$) may be required to measure velocity dispersions and disentangle the different inflow, outflow or rotating components.

Another feature of NGC 5394 is the high electron density of $n_e \sim 750$ cm $^{-3}$ in the central kpc, compared to the central $n_e \sim 200$ – 300 cm $^{-3}$ more typical of star-forming galaxies. This is not unique, e.g. Krabbe et al. (2014), in a Gemini Multi-Object Spectrograph study of 12 galaxies in 7 interacting pairs, found even lower [SII] 6717/6731 ratios and higher n_e (~ 1000 cm $^{-3}$) in some examples, (such as AM 1054-325B and AN 1219-430), and concluded that there was evidence interacting galaxies on average had higher n_e but, on the basis of moderate [OI]6300/ $H\alpha$ and [OIII]5007/ $H\beta$ ratios, this was not generally caused by shock excitation. Otherwise no cause was given except to attribute a central increase in n_e to gas inflow. The high central n_e of NGC 5394 could be a consequence of sustained gas infall over hundreds of Myr. Perhaps the n_e enhancement is maximised for this particular interaction geometry (coplanar, prograde, with larger companion) and stage. Large integral field surveys which can measure line ratios diagnostic of n_e will be able to quantify how it correlates with local and galaxy-scale properties.

8 CONCLUSIONS

(i) We examine CALIFA data for the spiral galaxy NGC 5394, which is strongly interacting with the $4\times$ more massive spiral NGC 5395. Most of the $H\alpha$ emission from NGC 5394, and therefore the star-forming activity, is concentrated in the nucleus (75% in the central $r \leq 1$ kpc) with additional star-forming regions in the SW of the disk and in two hotspots on the northern tidal arm. The galaxy is dusty, especially in the central $r \leq 1$ kpc where the $H\alpha$ / $H\beta$ ratio corresponds to a $H\alpha$ extinction of 2.32 magnitudes. For the whole galaxy we estimate a dust-corrected, $H\alpha$ based star-formation rate of 3.39 M $_{\odot}$ yr $^{-1}$ (Chabrier IMF). The outer northern-arm hotspot has only 0.9% of the total SFR but the highest $H\alpha$ equivalent width anywhere in the galaxy, over 100\AA . Isolated, extranuclear concentrations of star-formation, like this hotspot, are predicted to form in merger simulations.

(ii) Much of the galaxy outside the inner disk has a post-starburst spectrum with strong Balmer absorption ($\text{EW}_{\text{abs}}(H\delta) \geq 6\text{\AA}$). The $H\delta$ map and spectral model-fitting show the galaxy underwent an extensive episode of rapid star-formation 0.2–1.0 Gyr ago. Comparison with simulations and other mergers suggest this was triggered by the earlier close passage of the two galaxies.

(iii) NGC 5394 has a very high (for a purely star-forming galaxy) [NII]/ $H\alpha$ ratio of 0.63 at its centre. The

[OIII]/H β , [OI]6300/H α and [SII]/H α ratios remain low here, with no central peak, and thus disfavour AGN and shocks as explanations. Instead the enhanced central N2 ratio is probably due to increased collisional excitation associated with the very high central electron density, $n_e \simeq 750 \text{ cm}^{-3}$ on the basis of the [SII]6717/6731 ratio.

(iv) There is an outer region, forming an irregular ring of pixels around the nucleus at $9 < r < 16 \text{ arcsec}$ ($2.25 < r < 4 \text{ kpc}$), with even higher [NII]/H α ratios of 0.65–0.85, on average 0.74. Here the [OIII]/H β , [OI]6300/H α and [SII]/H α ratios are also high, suggesting a substantial ($\simeq 50\%$ of H α) contribution from shocks (we estimate, with $v \sim 250 \text{ kms}^{-1}$ and no pre-ionization).

(v) The O3N2 index of nebular metallicity with the lower, Marino et al. (2013) calibration and the mass-weighted model-fit stellar metallicity are similar at $12 + \log(\text{O}/\text{H}) \simeq 8.6$ (0.76 solar). The metallicity from the O3N2 index shows a negative radial gradient of about -0.03 dex/kpc (typical of disk galaxies) at $r < 10 \text{ arcsec}$ (or one r_{hl}), but this flattens at larger radii. Also the luminosity-weighted stellar metallicity is lower than the mass-weighted, especially in the outer disk, which might be the result of earlier inflow of lower metallicity gas.

(vi) The NaI(5890,5896) absorption in the spectrum of the nucleus has an equivalent width 6 to 7 Å, at least 3 times stronger than expected from stellar absorption alone, and is blueshifted by 3 Å over a $> 1.5 \text{ kpc}$ region. The residuals between the observed line and a stellar model indicate the non-stellar absorption component is blueshifted by 223 km s $^{-1}$. This is evidence for a neutral outflow of gas, at this velocity and perpendicular to the disk plane, driven by the central starburst.

(vii) Although the galaxy is viewed only $\sim 15^\circ$ deg from face-on, a velocity gradient is visible in the H α and [NII] emission lines, and in the stellar spectra (at least for the V1200 data), consistent with a disk rotation velocity $\sim 156\text{--}180 \text{ km s}^{-1}$ (as expected from the stellar mass). The H α and [NII] velocity maps are very similar and show no signature of an ionized outflow (such as a blueshifted region) either at the nucleus or the outer ring of high N2 ratios. This suggests that shocks in the outer high-excitation region are not produced by the central outflow but are more likely to be interaction-triggered gas infall within the disk plane.

(viii) The strong neutral gas outflow, high electron density and concentrated star formation ($> 1 \text{ M}_\odot \text{ yr}^{-1} \text{ kpc}^{-2}$) at the nucleus, and the strong Balmer absorption and hotspots elsewhere, are all a consequence of the prolonged interaction with NGC 5395. Over a timescale as long as $\sim 1 \text{ Gyr}$ and one or more perigalactica, this has reshaped the galaxy, formed tidal arms, triggered starbursts and gas inflow, and now the SFR may be increasing again as the two galaxies approach merger.

ACKNOWLEDGMENTS

This study uses data provided by the Calar Alto Legacy Integral Field Area (CALIFA) survey (<http://califa.caha.es/>), funded by the Spanish Ministry of Science under grant ICTS-2009-10, and the Centro Astronómico Hispano-Alemán. Based on observations collected at the Centro Astronómico Hispano Alemán (CAHA) at Calar Alto, operated

jointly by the Max-Planck-Institut für Astronomie and the Instituto de Astrofísica de Andalucía (CSIC).

NR, AH, JMG, PP and PL acknowledge Fundação para a Ciência e a Tecnologia (FCT) support through UID/FIS/04434/2013, and through project FCOMP-01-0124-FEDER-029170 (Reference FCT PTDC/FIS-AST/3214/2012) funded by FCT-MEC (PIDDAC) and FEDER (COMPETE), in addition to FP7 project PIRSES-GA-2013-612701. NR acknowledges the support of FCT postdoctoral grant SFRH/BI/52155/2013 followed by CAUP2014-04UnI-BPD (University of Porto). AH also acknowledges a Marie Curie Fellowship co-funded by the FP7 and the FCT (DFRH/WIIA/57/2011) and FP7 / FCT Complementary Support grant SFRH/BI/52155/2013. P.L. is supported by a Postdoctoral grant SFRH/BPD/72308/2010, funded by Fundao para a Cincia e a Tecnologia (FCT). JMG acknowledges support by the FCT through the Fellowship SFRH/BPD/66958/2009 and POPH/FSE (EC) by FEDER funding through the program Programa Operacional de Factores de Competitividade (COMPETE). PP is supported by FCT through the Investigador FCT Contract No. IF/01220/2013 and POPH/FSE (EC) by FEDER funding through the program COMPETE.

REFERENCES

- Allen M.G., Groves B., Dopita M., Sutherland R., Kewley L.J., 2008, ApJS 178, 20.
- Allende Prieto C., Lambert D.L., Asplund M., 2001, ApJ 556, L63.
- Arp H., 1966, ApJS 14, 1..
- Arp H., 1969, A&A 3, 418.
- Baldwin J.A., Phillips M.M., Terlevich R., 1981, PASP 93, 5.
- Barnes J.E., 2004, MNRAS, 350, 798.
- Barrera-Ballesteros J.K., et al., 2015, A&A accepted, arXiv:1505.03153.
- Belfiore F., et al. 2015, MNRAS 449, 867.
- Bordoloi R., et al., 2014, ApJ 794, 130.
- Calzetti D., Armus L., Bohlin R.C., Kinney A.L., Koornneef J., Storchi-Bergmann T., 2000, ApJ 533, 682.
- Cantó J., Elliott K.H., Meaburn J., Theokas A.C., 1980, MNRAS 193, 911.
- Casoli F., et al., 1998, A&A, 331, 451.
- Chen Yan-Mei, Tremonti C.A., Heckman T.M., Kauffmann G., Weiner B.J., Brinchmann J., Wang J., 2010, AJ 140, 445.
- Chien Li-Hsin, Barnes J.E., Kewley L.J., Chambers K.C., 2007, ApJ 660, 105.
- Cid Fernandes R., et al. 2013, A&A 557, 86.
- Cortese L., et al., 2014, ApJ 795, 37.
- Farage C.L., McGregor P.J., Dopita M.A., Bicknell G.V., 2010, ApJ 724, 267.

- García-Benito R., et al., 2015, *A&A*, 576, 135.
- García-Lorenzo B., et al. 2015, *A&A*, 573, 59.
- Gomes J.M., et al., 2015, *A&A*, submitted.
- Goto T., 2008, *MNRAS* 381, 187.
- Heckman T.M., Armus L., Weaver K.A., Wang J., 1999, *ApJ* 517, 130.
- Heckman T.M., Lehnert M.D., Strickland D.K., Armus L., 2000, *ApJS*, 129, 493.
- Higdon S.J.U, Higdon J. L., Smith B. J., Hancock M., 2014, *ApJ* 787, 103.
- Ho I-Ting, Kudritzki R-P, Kewley L.J., Jabran Zahid H., Dopita M.A., Bresolin F., Rupke D.S.N., 2015, *MNRAS* 448, 2030.
- Howell J.H., et al., 2010, *ApJ* 715, 572.
- Husemann B., et al., 2013, *A&A* 549, 87
- Kaneko H., Kuno N., Iono D., Tamura Y., Tosaki T.; Nakanishi K., Sawada T., 2013, *PASJ* 65, 20.
- Kauffmann, G. et al. 2003, *MNRAS*, 346, 1055
- Kaufman M., Brinks E., Elmegreen B.G., Elmegreen D.M.; Klarić M., Struck C., Thomasson M., Vogel S., 1999, *AJ* 118, 1577.
- Kaufman M., Sheth K., Struck C.; Elmegreen B.G., Thomasson M., Elmegreen D. M., Brinks E., 2002, *AJ* 123, 702.
- Kaufman M., Grupe D., Elmegreen B.G. Elmegreen D.M., Struck C., Brinks E., 2012, *AJ* 144, 156.
- Keel W.C., Kennicutt Jr. R.C., Hummel E., van der Hulst J.M., 1985, *AJ* 90, 108.
- Kennicutt Jr. R. C., 1998, *ARAA* 36, 189.
- Kewley L.J., Dopita M.A., Leitherer C., Davé R., Yuan T., Allen M., Groves B., Sutherland R., 2013, *ApJ*, 774, 100.
- Krabbe A.C., Rosa D.A., Dors O.L., Pastoriza M.G., Winge C., Hägele G.F., Cardaci M.V., Rodrigues I., 2014, *MNRAS* 437, 1155.
- Lanz L., et al., 2013, *ApJ* 768, 90.
- Le Tiran L., Lehnert M.D., van Driel W., Nesvadba N.P.H., Di Matteo P., 2011, *A&A* 534, 4.
- Lehmer B.D., Alexander D.M., Bauer F.E., Brandt W.N., Goulding A.D., Jenkins L.P., Ptak A., Roberts T.P., 2010, *ApJ*, 724, 559.
- López-Hernández J., Terlevich E., Terlevich R., Rosa-González D., Daz .; García-Benito R.; Vílchez J., Hägele G., 2013, *MNRAS* 430, 472.
- Marino R.A., et al., 2013, *A&A* 559, 114.
- Monreal-Ibero A., Arribas S., Colina L., Rodríguez-Zaurín J., Alonso-Herrero A., García-Marín M., 2010, *A&A* 517, 28.
- Papaderos P., et al., 2013 *A&A* 555, 1.
- Pettini M., Pagel B.E.J. 2004, *MNRAS*, 348, L59.
- Puerari I., Valdez-Gutiérrez M., Hernández-López I., 2005, *AJ* 130, 1524.
- Renaud F., Bournaud F., Duc P-A., 2015, *MNRAS*, 466, 2038.
- Rich J.A., Kewley L.J., Dopita M.A., 2011, *ApJ*, 734, 87.
- Rich J.A., Kewley L.J., Dopita M.A., 2014, *ApJ* 781, L12.
- Rich, J.A., Torrey P., Kewley L.J., Dopita M.A., Rupke D.S.N., 2012, *ApJ*, 753, 5.
- Rodríguez-Baras M., Rosales-Ortega F.F., Díaz A.I., Sánchez S.F., Pasquali A., 2014, *MNRAS* 442, 495.
- Rupke D.S.N., Kewley L.J., Barnes J.E., 2010, *ApJ* 710, 156.
- Sánchez S.F., et al. 2012, *A&A* 538, 8.
- Sánchez S.F., et al. 2014, *A&A* 563, 49.
- Sánchez S.F., et al. 2015, *A&A* 574, 47.
- Sánchez-Blazquez P., et al. 2014, *A&A* 570, 6.
- Sato T., Martin C.L., Noeske K.G., Koo D.C., Lotz J.M., 2009, *ApJ* 696, 214.
- Schweizer F., Seitzer P., 2007, *AJ* 133, 2132.
- Sobral D., Best P.N., Smail I., Mobasher B., Stott J., Nisbet D., 2014, *MNRAS* 437, 3516.
- Struck C., Kaufman M., Brinks E., Thomasson M., Elmegreen B.G., Elmegreen D.M., 2005, *MNRAS* 364, 69.
- Struck C., Smith, B.J., 2012, *MNRAS*, 422, 2444.
- Smith, B.J., Soria R., Struck C., Giroux M.L., Swartz D. A.; Yukita M., 2014, *AJ* 147, 60.
- Smith B.J., Struck C., Hancock M., Appleton P.N., Charmandaris V., Reach W.T., 2007, *AJ* 133, 791.
- Torrey P., Cox T.J., Kewley L., Hernquist L., 2012, *ApJ* 746, 108.
- Walcher C J., et al. 2014, *A&A* 569, 1.
- Wild V.; Groves B., Heckman T., Sonnentrucker P., Armus L., Schiminovich D., Johnson B., Martins L., Lamassa S., 2011, *MNRAS* 410, 1593.
- Wild V., Rosales-Ortega F., Falcon-Barroso J, et al., 2014, *A&A* 567, 143.
- Yuan T.-T., Kewley L.J., Swinbank A.M., Richard J., 2012, *ApJ* 759, 66.